Characterization of a patient-derived variant of GPX4 for precision therapy

Hengrui Liu[1], **Farhad Forouhar**[2,3], **Tobias Seibt**[4], **Russell Saneto**[5,6], **Kristen Wigby**[7,8], **Jennifer Friedman**[7,8,9,10], **Xin Xia**[2], **Mikhail S. Shchepinov**[11], **Sanath Ramesh**[12], **Marcus Conrad**[13,14], **Brent R. Stockwell**[1,2,3,15,*]

[1]Department of Chemistry, Columbia University, New York, NY 10027, USA

[2]Department of Biological Sciences, Columbia University, New York, NY 10027, USA

[3]Herbert Irving Comprehensive Cancer Center, Columbia University, New York, NY 10032, USA

[4]Department of Nephrology, Medizinische Klinik und Poliklinik IV, Klinikum der Universität München, 80336 München, Germany

[5]Division of Pediatric Neurology, Department of Neurology, University of Washington, Seattle, WA 98105, USA

[6]Center for Integrative Brain Research, Seattle Children's Hospital, Seattle, WA 98105, USA

[7]Department of Pediatrics, University of California, San Diego, CA 92093, USA

[8]Rady Children's Institute for Genomic Medicine, Rady Children's Hospital-San Diego, San Diego, CA 92123, USA

[9]Department of Neurosciences, University of California San Diego, La Jolla, CA, 92093, USA

[10]Division of Child Neurology, Rady Children's Hospital, San Diego, CA, 92123, USA

[11]Retrotope Inc, Los Altos, CA, USA.

[12]CureGPX4.org, Seattle, WA 98007, USA

[13]Helmholtz Zentrum München, Institute of Developmental Genetics, 85764 Neuherberg, Germany

[14]National Research Medical University, Laboratory of Experimental Oncology, Ostrovityanova 1, Moscow 117997, Russia

[15]Irving Institute for Cancer Dynamics, Columbia University, New York, NY 10027, USA

[*]Correspondence: bstockwell@columbia.edu.

Abstract

GPX4, as the only enzyme in mammals capable of reducing esterified phospholipid hydroperoxides within a cellular context, protects cells from ferroptosis. We identified a homozygous point mutation in the *GPX4* gene, resulting in an R152H coding mutation, in three patients with Sedaghatian-type spondylometaphyseal dysplasia (SSMD). With structure-based analyses and cell models, including patient fibroblasts, of this variant, we found that the missense variant destabilized a critical loop, which disrupted the active site and caused a substantial loss of enzymatic function. We also found that the R152H variant of GPX4 is less susceptible to degradation, revealing the degradation mechanism of the GPX4 protein. Proof-of-concept therapeutic treatments, which overcome the impaired R152H GPX4 activity, including selenium supplementation, selective antioxidants, and a deuterated PUFA were identified. In addition to revealing a general approach to investigating rare genetic diseases, we demonstrate the biochemical foundations for therapeutic strategies targeting GPX4.

Introduction

Sedaghatian-type spondylometaphyseal dysplasia (SSMD), first described in 1980, was reported as a rare neonatal lethal disorder characterized by severe metaphyseal chondrodysplasia with limb shortening, cardiorespiratory defects, and central nervous system abnormalities[1]. Most infants with SSMD succumb within days after birth due to respiratory distress[2]. To date, four SSMD-related *GPX4* variants have been described: c.476+5G>A, c.477–8_477–4del, c.270C>A (p.Tyr127*), and c.153_160del[3,4]. Considering the severe impact of these biallelic frameshifting or truncating mutations on GPX4 function, the clinical phenotypes of SSMD patients are likely due to complete loss of GPX4 enzymatic function, but the exact pathophysiological mechanism is unknown.

Glutathione Peroxidase 4 (GPX4) is a selenoprotein and a member of the glutathione peroxidase family of enzymes, which share an antioxidant function of reducing peroxides through the use of the co-substrate glutathione[5]. Despite the structural and functional similarities between these enzymes, GPX4 is distinct from other GPX enzymes, being the only enzyme in mammals capable of reducing esterified phospholipid hydroperoxides and cholesterol hydroperoxides within the context of cell membranes[5]. Therefore, when GPX4 activity is compromised, accumulation of lipid peroxidation products can disrupt membrane architecture, resulting in cell death through ferroptosis, an iron-dependent form of non-apoptotic cell death[6]. Accordingly, an essential role for GPX4 during embryogenesis and early development has been suggested by the failure of GPX4 homozygous knockout mice to survive past early gestation[7,8].

Here, we identified three individuals with mild SSMD features from two unrelated families who were found to harbor a recurrent homozygous point mutation in the *GPX4* gene, c.455 G>A (p. R152H), by whole exome sequencing. We sought to investigate the impact of this patient-derived *GPX4* missense variant on the function of GPX4 protein, to guide SSMD patients towards treatments. Furthermore, our structural examination into the variant suggested that K48 has an essential role in modulating GPX4 function, in addition to the previously reported catalytic triad (Sec46/Gln81/Trp136) and Asn137[9]. We further

found that the R152H variant alters the degradation of GPX4, revealing the degradation mechanism of GPX4 protein.

Results

R152H variant causes substantial loss of function

A recurrent homozygous R152H point mutation in the *GPX4* gene was identified in the whole exome sequencing of three patients with SSMD features (Supplementary Table 1). To investigate the impact of the R152H variant on GPX4 structure and function, we began with computational modeling of the GPX4^{R152H} protein structure. Substitution of Arg152 in the crystal structure of GPX4 by His was followed by a global minimization of the structure in an implicit solvent to generate a GPX4^{R152H} structural model.

Comparing GPX4^{R152H} with GPX4^{WT}, we found that the R152H variant significantly altered the surface around residue 152, as evidenced by the loss of a hydrophobic pocket centered on Arg152 in the wild-type protein (Fig. 1a). The change in the surface features mainly derived from a conformational change of the loop between Pro124 and Ala133, with which the long side chains of Arg152 formed multiple hydrogen bonds in the WT protein to support the loop in an open conformation, but not in the His variant, which has a short side chain and fewer H-bond donors such that the loop collapsed (Fig. 1b).

Molecular dynamics (MD) simulations of GPX4^{R152H} and GPX4^{WT} predicted this loop to be exceptionally mobile in the context of the variant (Fig. 1c). GPX4^{R152H} also exhibits additional flexibility in its active site (Supplementary Video 1 and 2). Accordingly, the average distance between the active site catalytic residue Sec46 and its catalytic partners Gln81/Trp136 was significantly increased in GPX4^{R152H} and presented a considerably wide distribution throughout timescale of the dynamics simulated, indicating a predicted weaker interaction among the catalytic triad (Fig. 1d).

As a control, GPX4^{R152R} was also generated by a synonymous mutation of Arg152 to Arg using the same method. Significant structural alterations caused by the R152H mutation were observed in a comparison of GPX4^{R152R} with GPX4^{R152H}, excluding artificial effects associated with the analysis (Extended Data Fig. 1 and 2a-b, Supplementary Video 3 and 4). In addition, the presence of waters in the MD simulation box significantly increased the mobility of the loop G126-T139 in GPX4^{R152H} as compared to water-free simulations, suggesting water alone is not enough to restore hydrogen bonds as to stabilize this loop (Supplementary Table 2, Supplementary Video 5 and 6).

To experimentally determine the impact of this variant in a human cell context, we established a cell model of the R152H mutation by stably overexpressing either GFP-tagged-GPX4^{WT} or GFP-tagged-GPX4^{R152H} in HT-1080 fibrosarcoma cells, in which GPX4 functions to protect cells from ferroptosis (Extended Data Fig. 3a). Using HT-1080 cells transfected with empty vector as a control, we measured the enzymatic activity of the transfected GFP-GPX4 protein via its ability to reduce a phospholipid hydroperoxide in an NADPH-coupled assay, as reported previously[10]. By normalization of enzyme activity to protein level, measured by western blot, we found that one unit of GPX4^{R152H} exhibited

~40% of the activity of GPX4^{WT} in this scenario (Fig. 2a and Extended Data Fig. 3b, c). To further confirm the variant-induced loss of activity in different genetic backgrounds and to exclude interference from endogenous WT GPX4, using *Gpx4*-knockout HT-1080 human cells and Pfa-1 murine cells, we overexpressed human or murine, WT or R152H exogenous GPX4[7,11–13]. We found that *Gpx4*-knockout cells expressing GPX4^{R152H}, similar to Gpx4-knockout cells, require α-tocopherol for normal growth, as they started to exhibit lower viability on day 7 after removal of α-tocopherol from the cell culture media, which is not the case for cells expressing GPX4^{WT}; this suggests a profound impact of the R152H variant on GPX4 function (Fig. 2b). To characterize this effect further, we measured GPX4 enzymatic activity of engineered *Gpx4*-knockout cells cultured in medium with or without α-tocopherol, in which we found an increasing loss of activity over time for R152H GPX4 without α-tocopherol (Fig. 2c, Extended Data Fig. 3d). Because the observed gradual loss of activity specifically for R152H GPX4 is correlated with the cell death timeline and is in advance of the viability decrease, it suggests that the accumulation of lipid peroxides caused by the less active R152H GPX4 will further deactivate R152H GPX4 and that incremental loss of activity eventually leads to compromised cell viability.

We therefore predicted that the characteristic reduction in enzyme activity in R152H GPX4 would result in impaired resistance to ferroptosis. Accordingly, we tested the ferroptosis sensitivity of HT-1080 cells overexpressing comparable level of GFP-GPX4^{WT} or GFP-GPX4^{R152H} (Extended Data Fig. 4a). While both cell lines were more resistant to ferroptosis induced by the GPX4 inhibitors RSL3, ML162 and by the system x_c^- inhibitor IKE, as compared to a cell line transfected with empty vector, overexpression of GPX4^{R152H} was less protective against ferroptosis inducers than was GPX4^{WT}, consistent with the lower activity of this variant protein for reducing lipid hydroperoxides (Fig. 2d).

Together, these data suggest that the partial loss of GPX4 phospholipid peroxidase activity caused by R152H alteration likely contributes to the overall pathological phenotype in SSMD patients harboring this variant. Additionally, since a relatively low level of cellular GPX4 activity provided by a small amount of WT GPX4 was reported to be sufficient for cell survival in some contexts, the R152H-specific vulnerability to deactivation by accumulation of lipid peroxide indicates a sensitivity of R152H GPX4 to overoxidation and therefore differentiates the lower activity of R152H GPX4 from equivalent activity provided by the WT GPX4[13]. Beyond the observed activity loss, considering the profound impact of R152H on GPX4, we suspect that R152H may also impact GPX4 function through additional mechanisms.

R152H causes a significant conformational change

To further understand why the alteration of a single amino acid residue distant from the active site caused a significant loss of enzymatic function in GPX4, we solved the x-ray crystal structure of GPX4^{U46C} and GPX4$^{U46C\_R152H}$ at 1.5 Å resolution (Extended Data Fig. 4b, c). The backbone of GPX4$^{U46C\_R152H}$ aligned well with GPX4^{U46C}, and the most significant change was in the loop between Pro124 and Ala133, which was intrinsically disordered in GPX4^{R152H}, as evidenced by the loss of electron density corresponding to these residues (Fig. 2e, f). As modeling has suggested, this change is likely due to the loss

of multiple hydrogen bonds that Arg152 forms with the backbone carbonyls of Gly126, Asn132 and Ala133, such that the loop becomes exceptionally flexible when this arginine is not present. This change is consistent with our observation that GPX4[U46C-R152H] exhibited a lower melting temperature than GPX4[U46C] ($T_m = -4°C$), which suggested R152H resulted in a conformational change of the GPX4 structure and significantly decreased thermal stability of GPX4 protein (Fig. 2g).

Moreover, since active site residue Trp136 is in this disordered loop, we examined the active site and found distances between pairs of the catalytic residues were increased, as expected from modeling (Extended Data Fig. 4d, e). While this observation may partly explain the decrease in catalytic activity, we also noticed in the x-ray structure a significant shift of the side chain of Lys48 away from the active site (Extended Data Fig. 4f). The exceptional mobility of Lys48 was also predicted by modeling. Since the positively-charged Lys48 features strong interactions with the active site selenium/sulfur anion in the structure of GPX4[WT] and our MD simulation of GPX4[U46C], we reasoned that Lys48 might have an important role in the enzymatic function of GPX4, and its departure from the active site may impair enzymatic activity (Supplementary Video 7)[14].

Lys48 has an essential role in modulating the GPX4 activity

To further investigate the role of Lys48 in the enzymatic function of GPX4, we generated HT-1080 cells stably overexpressing an alanine mutant of GPX4, GFP-GPX4[K48A], or GFP-GPX4[K48L], for which the mutation removed the positively charged ε-amino group on the side chain. Strikingly, we found that GPX4[K48A] had an almost complete loss of activity to reduce phospholipid hydroperoxides in this context, as its overexpression did not effectively increase the overall GPX4 activity in HT1080 cells, which is in contrast to the overexpression of WT GPX4 (Fig. 3a, Extended Data Fig. 5a). In contrast, we found that GPX4[K48L] featured an enhanced enzymatic activity, which is in line with a previous observation that the recombinant K48L mutant of GPX4 featured a higher catalytic activity than WT[14].

Correspondingly, while overexpression of GFP-GPX4[K48A] in HT-1080 cells did not show further protective effects in addition to endogenous GPX4 against ferroptosis induced by RSL3, overexpression of GFP-GPX4[K48L] was more protective than WT GPX4 against RSL3 (Fig. 3b, Extended Data Fig. 5b). These results suggested a profound and intriguing modulatory role of Lys48 on GPX4 activity.

To illuminate the mechanism for this essential modulation, we solved the crystal structures of GPX4[U46C_K48A] and GPX4[U46C_K48L] protein (Extended Data Fig. 5c, d). While the GPX4[U46C_K48A] and GPX4[U46C_K48L] proteins are stable and superimpose well upon the structure of GPX4[U46C] (Fig. 3c, d), MD simulations of these three structures revealed additional flexibility in the active site of GPX4[U46C_K48A], whereas an enhanced stability was observed in the active site of GPX4[U46C_K48L] (Supplementary Videos 7–9). Accordingly, the average distance between the active site catalytic residue Cys46 and its catalytic partners Trp136 was significantly increased in GPX4[U46C_K48A], which indicated a weaker interaction, while the average distance in GPX4[U46C_K48L] was even lower than in GPX4[U46C], which indicated a stronger interaction (Fig. 3e). Consistent results were

also observed in the MD simulations of computationally modeled Lys48 variants of WT selenocysteine-containing GPX4 (Extended Data Fig. 5e, Supplementary Video 10–12). This suggests that the interaction between Lys48 and (Seleno-)Cys46 modulates the conformation of the GPX4 active site and normally stabilizes the active site to be in a more compact and functional state, and that this feature is impaired when Lys48 is mutated to Ala.

To further study the role of Lys48 in the context of the canonical catalytic cycle of the GPX4 enzymatic reaction, in which the first step is the oxidation of GPX4 by its hydroperoxides substrates, we solved the crystal structure of fully oxidized GPX4^{U46C}, where the sulfur of Cys46 was oxidized to sulfonic acid (SO$_3$H, Extended Data Fig. 5f). We found that Lys48 is positioned in close proximity (3.6 Å distance) to the oxidized Cys46, even closer than to reduced Cys46 (5.2 Å distance) in the crystal structure of reduced GPX4^{U46C} (Fig. 3f). This close proximity was also previously observed in the structure of oxidized selenocysteine-containing GPX4[14]. This suggests a role for Lys48 in the modulation of the active site in the oxidized state of GPX4. To further investigate this interaction, we performed MD simulations of fully oxidized GPX4^{U46C}, GPX4$^{U46C\_K48A}$, and GPX4$^{U46C\_K48L}$ and found that oxidized GPX4^{U46C} exhibited additional flexibility in the active site, which suggests the oxidized active site to be in an open state. However, oxidized GPX4$^{U46C\_K48A}$ and GPX4$^{U46C\_K48L}$ featured extreme stability (Fig. 3g, Supplementary Videos 13–15). Since the SeO$_3^-$/SO$_3^-$ state of GPX4 is inactive and irreversibly overoxidized, especially for the sulfur variant[11], the stability of the K48A mutant in this state might contribute to its loss of activity.

The second step in the catalytic cycle of GPX4 is the incorporation of its cofactor GSH via the formation of a Se-S bond, which prepares oxidized GPX4 for regeneration to the reduced form. Therefore, we covalently docked GSH into the crystal structures of GPX4^{U46C}, GPX4$^{U46C\_K48A}$, GPX4$^{U46C\_K48L}$, and the computationally modeled structures for Lys48 variants of WT GPX4, and obtained highest covalent-docking affinities with GPX4^{U46C} or GPX4^{WT}, both of which featured Lys48 (Extended Data Fig. 6a, Supplementary Table 3)[15]. This is in line with a previously reported study that proposed a role of Lys48 in interacting with GSH[16]. Additionally, the flexible and open active site of oxidized GPX4^{U46C}, as found during its MD simulation, might also be more accessible for GSH to incorporate and reduce oxidized GPX4.

The above analysis suggested an elevated susceptibility of K48L to overoxidation, in spite of its higher initial activity, as loss of the positively charged ε-amino group in the K48L mutant might have a significant impact on its interaction with the negatively charged oxidized active site or the GSH cofactor. To validate our analysis, we tested the sensitivity of HT-1080 cells overexpressing comparable level of GFP-GPX4^{WT} or GFP-GPX4^{K48L} to ferroptosis induced by system x$_c^-$ inhibitor IKE, which depleted cellular GSH and may therefore cause overoxidation of GPX4; we found that overexpression of GFP-GPX4^{K48L} in HT-1080 cells did not show further protective effects in addition to the endogenous GPX4 against IKE (Fig. 3h, Extended Data Fig. 6b).

In addition to K48A and K48L, we computationally modelled additional Lys48 variants of WT GPX4 and performed the above analysis on K48E (negative charge), K48Q (hydrogen

bond), and K48R (positive charge and hydrogen bond). The broad spectrum of performance observed on these Lys48 variants further supported the profound modulatory role of Lys48 on GPX4 activity (Extended Fig. 5e, Supplementary Table 3, Supplementary Video 16–18).

In summary, these data reveal a multi-pronged mechanism for the modulation of GPX4 enzymatic activity by Lys48: to stabilize the active site to be in a more compact and functional state, to modulate the oxidized active site for cycling, and to facilitate the incorporation of the cofactor GSH. Therefore, the shift of Lys48 away from the active site in GPX4^{R152H} may contribute to the partial loss of function and specific sensitivity to overoxidation observed with GPX4^{R152H}.

R152H variant is resistant to degradation

When we tested the ferroptosis sensitivities of HT-1080 cells overexpressing GFP-GPX4^{R152H} or GFP-GPX4^{WT}, we were surprised to find that GPX4^{R152H} provided comparable protection as GPX4^{WT} to the ferroptosis inducer FIN56, despite insufficient protection against RSL3, ML162 and IKE (Fig. 4a, Extended Data Fig. 7a). Since FIN56 was reported to induce ferroptosis via promoting the degradation of GPX4, as well as depleting coenzyme Q_{10}, we speculated that R152H may change the susceptibility of GPX4 to degradation[17]. Therefore, we treated HT-1080 cells overexpressing GFP-GPX4^{R152H} or GFP-GPX4^{WT} with various ferroptosis inducers and measured the residual GPX4 protein level after treatment by western blot, using methods reported previously (Extended Data Fig. 7b)[18]. The endogenous GPX4 protein served as internal control and confirmed that RSL3, ML162 and FIN56 significantly promoted degradation of GPX4 under these treatment conditions (Fig. 4b, Extended Data Fig. 7c, d). Meanwhile, significant degradation of transfected GFP-GPX4^{WT} was induced by RSL3, ML162, and FIN56, as expected, which excluded interference of the GFP tag on the degradation (Fig. 4c, Extended Data Fig. 7e). We observed that GFP-GPX4^{R152H} was more resistant compared to GFP-GPX4^{WT} to degradation induced by RSL3, ML162, and FIN56 (Fig. 4d, Extended Data Fig. 7f). We further conducted cycloheximide-chase analyses of WT and R152H GFP-GPX4 under RSL3 treatment, which verified the increased half-life of R152H GPX4 under this condition (Fig. 4e, Extended Data Fig. 8a).

The mechanism of GPX4 degradation induced by RSL3 and FIN56 is not clear, despite some efforts to understand this phenomenon[17,19]. Based on our finding that the loop between Pro124 and Ala133, which contains Lys125 and Lys127, exhibits extra flexibility in the context of GPX4^{R152H}, we developed a hypothesis that RSL3-induced or FIN56-induced GPX4 degradation involves a proteasome-dependent mechanism, with Lys125 and Lys127 as potential ubiquitination sites on GPX4; in this model, these highly mobile lysine residues in R152H hinder ubiquitination and prevent degradation. We tested this hypothesis by examining GPX4 degradation in HT-1080 cells stably overexpressing GFP-GPX4$^{K125R\_K127R}$, where the proposed sites of ubiquitin ligation were removed by point mutations. While endogenous GPX4 was degraded upon treatment with RSL3, ML162, or FIN56, we found that GFP-GPX4$^{K125R\_K127R}$ was resistant to degradation, even more so than the R152H mutant (Fig. 4f, Extended Data Fig. 8b, c). Together, these data suggest that the degradation of GPX4 induced by RSL3 and FIN56 involves a proteasome-dependent

mechanism, and that Lys125 and Lys127 of GPX4 are key sites of ubiquitination. An alternative approach to modulate GPX4 for clinical applications was thus revealed.

Impact of R152H variant is similar in patient fibroblasts

To validate the observations regarding the R152H variant, fibroblasts developed from a patient with homozygous R152H variants (RAG01, $GPX4^{R152H/R152H}$) and the patient's parent as an unaffected control with heterozygous genotype (RAG02, $GPX4^{R152H/WT}$) were tested. Although the two human fibroblast cell lines expressed an equivalent level of GPX4 protein based on western blot analysis, RAG01 cells exhibited a significantly lower level of GPX4 enzymatic activity than RAG02, confirming that R152H variant in GPX4 caused partial loss of enzymatic function (Fig. 5a, b). As expected, RAG01 with a partial loss of GPX4 activity was found to be more sensitive than RAG02 to lipid peroxidation and to ferroptosis induced by RSL3, ML162, IKE, and FIN56 (Fig. 5c).

We then tested the degradation vulnerability of GPX4 protein in both fibroblast cell lines, and found that the R152H variant altered the degradation of GPX4, such that $GPX4^{R152H}$ in RAG01 was more resistant than the combination of $GPX4^{WT}$ and $GPX4^{R152H}$ in RAG02 to degradation induced by RSL3 and ML162, further suggesting the involvement of ubiquitin-proteasome system in GPX4 degradation (Fig. 5d). Moreover, imaging of fibroblast cells with GPX4 immunofluorescence and DAPI staining under confocal microscopy showed an indistinguishable level of cellular GPX4 intensity in RAG01 and RAG02 (Fig. 5e). Additionally, the ratio of cytoplasmic GPX4 to nuclear GPX4 was comparable in RAG01 and RAG02, indicating that alteration of GPX4 subcellular localization was not observed for this patient-derived variant (Fig. 5f, g). However, we found that cells undergoing mitosis exhibited a much higher fluorescence intensity of GPX4 than non-mitotic cells. This indicated that, during proliferation, fibroblast cells express a high level of GPX4 protein to protect themselves against lipid peroxidation. The loss-of-activity variant in GPX4 might therefore partially suppress mitosis or cause cell death during mitosis, as evidenced by the lower number of RAG01 cells than RAG02 cells when seeded equivalently.

Identification of proof-of-concept treatment

The results described above demonstrated that the patient-derived R152H variant of GPX4 caused partial loss of its function in phospholipid peroxidase activity and therefore is pathological. However, the data also suggested that the overexpression of the partially-active but degradation-resistant $GPX4^{R152H}$ in HT-1080 cells did increase the resistance of cells to ferroptosis induced by lipid peroxidation, though less effectively than wild-type GPX4 (Fig. 2d). Therefore, we developed a hypothesis that boosting the expression level of the R152H variant of the selenoprotein GPX4 via selenium supplementation might compensate for the partial loss of enzymatic function. This hypothesis is based on the observation that selenium supplementation can significantly increase the expression level of the selenoprotein GPX4, up to 48-fold, as well as the expression of another anti-oxidant selenoprotein, GPX1, up to 40-fold, in human cells[20]. Additionally, selenium is readily available from dietary source such as Brazil nuts and as over the counter (OTC) supplement tablets[21].

We first tested this selenium treatment hypothesis on fibroblasts derived from the patient. Accordingly, we found that sodium selenite, selenomethione, and methylselenocysteine could boost the viability of patient fibroblast RAG01 slightly to 138%, 138%, and 137%, with an EC_{50} value of 0.8 nM, 0.4 nM, and 0.9 nM, respectively (Fig. 6a-b, Extended Data Fig. 9a). The similarity in the extent of viability increase for these three selenocompound treatments suggested a consistency of selenium supplementation, and their shared low EC_{50} values indicated their high potencies as treatments. As the CC_{50} of sodium selenite toxicity (12 μM) was 15,000-fold higher than the its EC_{50}, the avoidance of its toxicity should be manageable in patients, while selenomethione and methylselenocysteine might be preferred due to their lack of toxicity. It was also noteworthy that the rescue effect of selenium was specific for RAG01, with relatively minimal effect on the control RAG02 line.

Moreover, we included N-acetylcysteine and N-acetylcysteine-amide in the test, which might also benefit patients, as metabolic precursors for the GPX4 cofactor GSH[22]. We found that N-acetylcysteine and N-acetylcysteine-amide could boost the viability of RAG01 cells slightly to 118% and 116%, which were less effective than selenocysteine (Fig. 6c, Extended Data Fig. 9b). This suggested the utility of selenium for patients with compromised GPX4 activity, and that the elevation of GSH level in cells might be helpful in boosting the activity of GPX4.

Additionally, we evaluated the lipophilic antioxidants α-tocopherol, CoQ_{10} and idebenone (a soluble analog of CoQ_{10}), and found that they can also boost the viability of RAG01 cells to 250 %, 197 %, and 245 %, with EC_{50} values of 115 nM, 5 μM, and 228 nM, respectively (Fig. 6d-f). We also found that dimethyl fumarate, an Nrf2 activator that promotes an antioxidant response, boosted the viability of RAG01 slightly to 127% (Fig. 6g)[23]. These results suggests that lipophilic antioxidant supplements may be useful for patients with the R152H GPX4 variant, and possibly dimethyl fumarate to a limited extent.

Finally, we found that treatment with deuterium-reinforced linoleic acid (RT-001), a polyunsaturated fatty acid (PUFA) with deuterium at its bis-allylic site to inhibit lipid peroxidation, provided the most pronounced rescue effect on RAG01 (440%, Fig. 6h)[18,24–26]. In contrast, normal linoleic acid exhibited a toxicity effect to RAG01 at high concentrations, which suggested the likely involvement of lipid peroxidation in the compromised cell viability observed on patient cells (Fig. 6i).

To further evaluate the potency of the proof-of-concept treatments and compare effects on $GPX4^{R152H}$ to a control expressing wild-type GPX4 (instead of RAG02 expressing both wild-type and the variant), we tested all treatments on Gpx4-knockout Pfa-1 cells that were transfected to overexpress human/murine $GPX4^{WT}$ or $GPX4^{R152H}$ (Extended Data Fig. 9c, 10). Ferrostatin-1, a radical trapping inhibitor of lipid peroxidation and ferroptosis, was also included in this test; its significant and selective rescue effect on cells solely expressing $GPX4^{R152H}$ demonstrated the involvement of lipid peroxidation and possibly ferroptosis in R152H GPX4 pathology. Proof-of-concept treatments effective on patient fibroblast cells also exhibited consistent rescue effects on the Pfa-1 cells, especially for α-tocopherol, CoQ_{10}, idebenone, and RT-001.

In summary, the observation that selenium supplementation, ferroptosis inhibitors, and antioxidants can increase cell number and viability of patient fibroblasts and R152H GPX4 cell models was consistent with the conclusion that the partial loss-of-function R152H mutation in GPX4 sensitizes patient cells to lipid peroxidation. Therefore, we expect that a combination treatment of selenium supplementation to boost R152H GPX4 level and lipophilic antioxidants (α-tocopherol and/or CoQ_{10}) with D-PUFAs such as RT-001 to suppress lipid peroxidation might be the most effective treatments, some of which are widely available as supplements, and may be therapeutically beneficial for patients with the R152H variant in GPX4.

Discussion

Prior to this study, previously reported patients with SSMD were identified to have predicted loss of function variants based on *in silico* data alone; these variants were not studied experimentally[3,4]. Our report provided evidence of the association of biallelic variants in GPX4 with SSMD. In addition, this report extends the phenotype associated with SSMD to include long-term survival beyond infancy.

This study began by examining the effect of the R152H missense mutation on GPX4, which adversely changed the protein structure and caused a partial loss of its antioxidant activity. As a hypomorphic allele, we therefore hypothesize that there is sufficient enzymatic function to allow for survival beyond infancy, but impaired proliferation and increased susceptibility to lipid peroxidation, ferroptosis, tissue damage, and degeneration. This finding would be in keeping with observations of the adult conditional *Gpx4* knockout mouse, which exhibited perinatal lethality, seizures, ataxia and progressive neuronal loss[7,27,28].

During our analysis, we used a structure-based computational modeling approach to study the effect of the variant on protein structure *in silico*, the predictions from which were confirmed by protein crystal structures and cellular assays. These experiments suggested the feasibility of structure-based modeling of variant protein structures to dissect the impact of patient-derived variants. The low-cost and high-throughput of computational modeling would potentially benefit more patients with orphan diseases or variation in key genes.

This R152H variant unexpectedly revealed the structural basis of GPX4's enzymatic activity and the regulation of its degradation: Lys48 was found to modulate GPX4 enzymatic activity and Lys125/Lys127 were revealed as sites of ubiquitin ligation. In addition, our study of R152H also suggested Arg152 as an allosteric site indirectly regulating GPX4 activity. Since recent studies highlighted GPX4 protein as an *Achilles's heel* of drug-resistant and metastatic cancers, which are exceptionally dependent on the GPX4 lipid peroxide repair pathway, we would expect biochemical therapeutic strategies targeting the essential residue Lys48 and allosteric site Arg152 or taking advantage of its degradation mechanism, to be developed as a high priority and benefit additional patients[29–31].

Methods

Patient Cohorts

In this study, we identified three individuals with SSMD (Sedaghatian type Spondylometaphyseal Dysplasia) features who were found to harbor a recurrent homozygous R152H point mutation in the *GPX4* gene.

At the age of 5 months, Patient 1 (Family 1) was diagnosed on brain auditory evoked responses (BAER) testing to have neurosensory hearing loss. The metabolic bone clinic suggested metaphyseal dysplasia. Whole-exome sequencing of Patient 1 and his parent was conducted. There was only one gene variant identified, c.455 G>A (p. R152H) of *GPX4*, which was found to segregate in each parent and presented in the patient as a homozygous biallelic variant.

A skeletal survey of Patient 2 (Family 2) at the age of 7 years revealed flaring of the proximal tibial metaphysis as well as distal femoral metaphysis, brachycephaly, moderate thoracolumbar levoscoliosis, coxa valga, thin and elongated second metatarsals, and diffuse osteopenia with thinning of the long bones. Patient 3 (Family 2) is the younger sister of Patient 2. Patient 3 did not pass her newborn hearing screen and subsequent brainstem auditory evoked response testing revealed bilateral auditory neuropathy. Whole-exome sequencing was also obtained clinically on Family 2, which reported the same variant in *GPX4* as Family 1.

See Supplementary Note for clinical observations for the three patients. All three patients and their families (Patient 1 from Family 1, and Patient 2 and 3 from Family 2) gave informed consent for genetic and clinical investigation. Both families were enrolled in an institutional approved study of children with undiagnosed neurogenetic disorders (Genomic Sequencing in Neurological Disorders research protocol, UCSD IRB #170437). Tissue samplings (including skin biopsy for the development of fibroblasts RAG01 and RAG02) and clinical observations of Patient 1 and his parent were approved by IRB #00002259 (Molecular and Biochemical Analysis of Metabolic Disorders, University of Washington). Study of GPX4 variant in the human fibroblast samples was approved by IRB #AAAS9249 (Evaluation of GPX4 variant activity in fibroblasts, Columbia University). Compensation was not provided.

Whole-exome sequencing

Whole-exome sequencing (WES) of all three patients was performed at GeneDx. Ages at sequencing were 9 months old for Patient 1 (male, May 2019), 7 years old for Patient 2 (male, Dec 2015), and 10 months old for Patient 3 (female, Dec 2015). Agilent clinical research exome kit was used for DNA fragment capture. NextGen sequencing (massive parallel sequencing) was performed on HiSeq platform (Illumina). Exome GRCh37/hg19 was applied as reference in custom analysis tool Xome Analysis to detect patient-derived variant. WES results were summarized in Supplementary Table 1.

Cell lines

HT1080 cells were obtained from ATCC and grown in DMEM with glutamine and sodium pyruvate (Corning 10–013) supplemented with 10% FBS, 1% non-essential amino acids (Invitrogen) and 1% penicillin-streptomycin mix (Invitrogen). The Tam-inducible $Gpx4^{-/-}$ murine embryonic fibroblasts (PFa1 MEFs) were used as described previously[7,11–13]. $Gpx4^{-/-}$ Pfa1 cells were grown in DMEM supplemented with 10% FBS, 1% glutamine, 1% penicillin-streptomycin mix, 750 μg/ml neomycin, 1 μM puromycin, and 1 μM tamoxifen. $Gpx4^{-/-}$ HT1080 cells were grown in DMEM supplemented with 10% FBS, 1% glutamine, 1% penicillin-streptomycin mix, 750 μg/ml neomycin. We found that $Gpx4$-knockout cells solely expressing GPX4^{R152H}, similar to $Gpx4$-knockout cells, required α-tocopherol for normal growth. So α-tocopherol was supplemented in the culture media of Gpx4-knockout cells solely expressing GPX4^{R152H}. However, it is noteworthy that the overoxidation and deactivation of R152H GPX4 by lipid peroxides would be artificially masked by the lipophilic antioxidant α-tocopherol, which may directly reduce the oxidized form of the GPX4 active site (selenenic or seleninic form), as demonstrated by the slightly higher activity of R152H GPX4 in cells cultured in medium with α-tocopherol (Fig. 2c).

Human fibroblast cell line RAG01 and RAG02 were developed from the patient with the homozygous R152H variant and his parent heterozygous for the R152H variant. As of sample collection, the patient (male, RAG01) was 22 months old, while his parent (male, RAG02) was 31 years old. RAG01 and RAG02 were grown in DMEM with glutamine and sodium pyruvate (Corning 10–013) supplemented with 15% FBS, 1% non-essential amino acids (Invitrogen), 1% penicillin-streptomycin mix (Invitrogen). Similar to $Gpx4$-knockout cells overexpressing R152H GPX4, patient fibroblast cells, RAG01, also required α-tocopherol for normal growth at low seeding densities; thus, α-tocopherol (10 μM) was supplemented in the medium for fibroblast cell lines and was only removed in advance of testing cellular viabilities. So it is noteworthy that, although the loss of GPX4 activity caused by R152H in fibroblasts appeared to be to a lesser extent than what we observed in the previous cell models, this not only might be because the control line RAG02 also expressed R152H GPX4, but also because fibroblast cells were cultured in medium supplemented with α-tocopherol, which was able to artificially mask the deactivation of R152H GPX4 by lipid peroxides (Fig. 5b). RAG01 and RAG02 cell lines are available for both commercial and academic use through CureGPX4.org, a patient organization dedicated to finding a treatment for SSMD disease.

Cells were maintained in a humidified environment at 37 °C and 5% CO_2 in a tissue incubator.

Computational Modeling and Molecular Dynamics (MD) simulation

In silico residue mutation analysis, molecular dynamics (MD) simulations, and ligand docking were performed in Maestro (Schrödinger Suite). Since all variants of the GPX4 protein that we physically purified *in vitro* (GPX4^{R152H}, GPX4^{K48A}, and GPX4^{K48L}) has the U46C mutation to aid protein expression, we started from computational modeling on GPX4 with the U46C mutation *in silico* to either directly compare our crystal structures of GPX4 protein (GPX4^{R152H}) to the computationally predicted GPX4^{R152H} structure side by

side, or use our crystal structures of GPX4 protein (GPX4^{K48A} and GPX4^{K48L}) as starting points for MD simulations. We then performed computations on GPX4^{WT} structure (PDB: 6HN3) as a confirmatory control to rule out possibilities of artificial effects caused by the U46C mutation. Eventually, consistent results were observed, regardless of using GPX4^{U46C} or GPX4^{WT} as input.

To model the structure of GPX4^{R152H}, the crystal structure of GPX4^{U46C} (PDB: 2OBI) and GPX4^{WT} (PDB: 6HN3) were imported into Maestro, preprocessed to remove water and add hydrogens, optimized at pH 7 for H-bond assignment, and minimized in the OPLS3e force field using Protein Preparation Wizard. Substitution of the Arg152 residue in the structure by His was followed by a global minimization of the whole structure in an implicit solvent to generate the R152H model. As a control, GPX4^{R152R} was also generated by a synonymous mutation of Arg152 to Arg using the same algorithm and minimization method to rule out possibilities of artificial effects caused by the computation process. For models that featured the U46C mutation, the cysteine thiol of C46 was manually set to a thiolate anion to mimic the active form of the enzyme, as the selenocysteine in which has a lower pKa and would convert to anion form in physiological conditions. SiteMap was then run under the default setting. A structural comparison between GPX4^{R152H} and GPX4^{R152R} was performed thereafter.

To further study the impact of R152H mutation with MD simulation, each of the above modeled structures was set up in an orthorhombic box with 0.15 M NaCl in SPC solvent and OPLS3e force field, unless otherwise noted. Multiple independent MD simulations of each system for 100 ns with 4.8 ps per step at 300 K and 1.01325 bar were performed with random seeding in Desmond Molecular Dynamics. Trajectories were recorded and analyzed. Simulation quality and event analysis were also done by Desmond. Videos for representative simulation process were exported.

It is noteworthy that the GPX4^{R152H} crystal structure that we solved (PDB: 7L8L) was not used for MD simulation because the loop between P124 and A133 does not exhibit a defined structure, which would complicate the modeling. It is also noteworthy that previously published crystal structure of GPX4^{U46C} (PDB: 2OBI) was used above to model GPX4^{R152H} structure. This is because this modeling was done before all other experiments in wet lab, including the acquisition of our own crystal structure of GPX4^{U46C} (PDB: 7L8K). Later, we found the structure of GPX4^{U46C} (PDB: 7L8K) that we solved is consistent with the previously reported structure (PDB: 2OBI). We then used 7L8K for all the following computational work.

To study the impact of K48 mutations on reduced GPX4, the GPX4^{U46C} (PDB: 7L8K), GPX4$^{K48A\_U46C}$ (PDB: 7L8R) and GPX4$^{K48L\_U46C}$ (PDB: 7L8M) crystal structures that we solved were respectively set up in an orthorhombic box and analyzed with MD simulations in the same protocol as noted above. Additional K48 variants modeled from GPX4^{WT} were also analyzed in the same protocol.

To study the impact of K48 mutations on oxidized GPX4, the fully-oxidized GPX4^{U46C} crystal structure (PDB: 7L8Q) that we solved was not used for MD simulation. Instead,

for side-by-side comparison, we manually set the cysteine thiol of C46 in GPX4^{U46C} (PDB: 7L8K), GPX4$^{K48A\_U46C}$ (PDB: 7L8R) and GPX4$^{K48L\_U46C}$ (PDB: 7L8M) to be fully oxidized. After confirmation of the relevance of the modeled oxidized structure by comparing it to crystal structure, we used these fully oxidized structures in MD simulation, in the same way as described above.

Additionally, covalent docking of GSH was performed on the crystal structures of GPX4^{U46C} (PDB: 7L8K), GPX4$^{K48A\_U46C}$ (PDB: 7L8R), and GPX4$^{K48L\_U46C}$ (PDB: 7L8M), which were solved and reported in this work. Other docking receptors of GSH are the crystal structure of GPX4^{WT} (PDB: 6HN3) and modeled structures based on it.

Generation of HT1080 Cells Expressing tagged GPX4

A pBabe-puro vector incorporated with the cDNA of GFP-tagged-cyto-GPX4^{WT} was prepared in previous work (pBP-GFP-cGPX4^{WT})[6]. With the vector as template, the following mutagenesis primers were designed using the Agilent QuikChange Primer Design application: R152H (5'- CTG CGT GGT GAA GCA CTA CGG ACC CAT GG –3', 5'- CCA TGG GTC CGT AGT GCT TCA CCA CGC AG –3'), K48A (5'- GGC CTC CCA GTG AGG CGC GAC CGA AGT AAA CTA C –3', 5'- GTA GTT TAC TTC GGT CGC GCC TCA CTG GGA GGC C –3'), K125R_K127R (5'- TGG ATG AAG ATC CAA CCC AGG GGC AGG GGC ATC CTG –3', 5'- CAG GAT GCC CCT GCC CCT GGG TTG GAT CTT CAT CCA –3'). Primers were purchased from Integrated DNA Technologies. Site-directed mutagenesis kit (QuickChange II, Agilent 200521) was then used to acquire pBP-GFP-cGPX4^{R152H}, pBP-GFP-cGPX4^{K48A}, and pBP-GFP-cGPX4$^{K125R\_K127R}$. K48L mutation was conducted by GENEWIZ mutagenesis service on the same template vector to acquire pBP-GFP-cGPX4^{K48L}. All resulted plasmids were confirmed by sequencing at GENEWIZ.

HT-1080 cells were seeded into a 6-well dish at a density of 300,000 cells/well the night before lipofection. 2.5 μg DNA (empty pBabe-puro vector and the above five GFP-GPX4 expressing pBabe-puro vectors, separately), 7.5 μL Lipofectamine 3000 (Invitrogen, L3000015), and 250 μL Opti-MEM were incubated for 5 min at room temperature before adding to the HT-1080 cells. Following transfection, cells were passaged several times in HT1080 media containing 1.5 mg/mL puromycin and grown in this media for all experiments performed. Expression of the exogenous GFP-tagged-GPX4 was confirmed with fluorescence microscope and Western Blot with both GFP and GPX4 antibodies.

Western Blot

For the quantification of cellular GPX4 protein level for the GPX4-specific activity assay, the biological duplicates of each cell line subject to the GPX4-specific activity were tested by Western Blot in technical duplicates, which made a total of 4 samples for each cell line. In particular, cells were harvested with trypsin (Invitrogen, 25200–114), pelleted, and lysed by LCW lysis buffer (0.5 % TritonX-100, 0.5 % sodium deoxycholate salt, 150 mM NaCl, 20 mM Tris-HCl pH 7.5, 10 mM EDTA, 30 mM Na-pyrophosphate, and cOmplete protease inhibitor cocktail). While part of the cell lysates was blotted for protein quantification, the other part of lysates was used for the GPX4-specific activity assay.

For the GPX4 degradation study, cells were seeded at 800,000 per well in a 60-mm plate and allowed to adhere overnight. Cells were then treated with 100 μM α-tocopherol and either 1 μM RSL3, 1 μM ML162, 10 μM IKE, 10 μM FIN56, or vehicle for 10 h before harvest. Particularly for cycloheximide chase analysis, cells were treated with 4 μM RSL3, 30 μg/ml cycloheximide, and 100 μM a-Tocopherol for 0, 2, 4, or 6 hours before harvest. Each condition was performed for at least duplicates. Cells were harvested with trypsin (Invitrogen, 25200–114), pelleted, and lysed with RIPA buffer.

For both experiments, Western Blot of each condition or cell line was performed for at least duplicates. Cell lysates were blotted and imaged as previously described[6]. Antibodies used were GPX4 (Abcam, ab125066, 1:250 dilution), GFP (Santa Cruz, sc-9996, 1:1000 dilution), actin (Cell Signaling, D18C11, 1:3,000 dilution), GAPDH (Santa Cruz, sc-47724, 1:10,000 dilution), IRDye® 800CW Goat anti-Rabbit IgG Secondary Antibody (LI-COR, #926–33221, 1:5,000), and Goat anti Mouse IgG (H+L) Secondary Antibody conjugated with Alexa Fluor 680 (Thermo Fisher Scientific Cat# A-21057, 1:5,000). Results were quantified using a LI-COR Odyssey CLx IR scanner and ImageJ, and plotted with GraphPad Prism.

Determination of GPX4-Specific Activity

We applied a NADPH-coupled cellular GPX4 enzymatic activity assay as previously reported[10]. Oxidized glutathione, generated by GPX4 during reducing its specific phospholipid hydroperoxides substrate, was reduced by Glutathione Reductase at the expense of NADPH, the decrease in the characteristic absorbance of which at 340 nm was monitored and quantified as GPX4 activity. The GPX4-specific substrate PCOOH was prepared by enzymatic hydroperoxidation of phosphatidylcholine by soybean lipoxidase type IV: 22 mL of 0.2 M Tris-HCl, pH 8.8, containing 3 mM sodium deoxycholate and 0.3 mM phosphatidylcholine was incubated at room temperature, under continuous stirring, for 30 min with 0.7 mg of soybean lipoxidase type IV. The mixture was loaded on a Sep-Pak Cl8 cartridge (Waters-Millipore) washed with methanol and equilibrated with water. After washing with 10 volumes of water, phosphatidylcholine hydroperoxides were eluted in 2 mL of methanol.

To measure the GPX4 activity for specific cell lines of interest, 48 million cells of each cell line were harvested and lysed by LCW lysis buffer (0.5 % TritonX-100, 0.5 % sodium deoxycholate salt, 150 mM NaCl, 20 mM Tris-HCl pH 7.5, 10 mM EDTA, 30 mM Na-pyrophosphate, and complete protease inhibitor cocktail). The concentration of protein in the lysate was determined using BCA assay kit using BSA as standards. Then, on a 96-well plate, 250μL 1.5 μg/μL cell lysate was incubated in the GPX4 activity assay buffer (0.1 % Triton X-100, 100 mM Tris-HCl pH 7.4, 10mM NaN_3, 5 mM EDTA, 0.6 IU/mL Glutathione reductase, 0.5 mM NADPH) at 37°C for 10 min. PCOOH was then added to the mixture to initiate GPX4 reaction. Absorbance of NADPH at 340 nm was determined kinetically at 1 min interval over the 20 min time. GPX4 activity was calculated based on the assumption rate of NADPH during this kinetic process. Experiments using lysis buffer instead of cell lysate and controls without addition of PCOOH were also done to measure the particular activity of GPX4 to reduce phospholipid hydroperoxides. Total GPX4 activity

of each sample were normalized to their specific GPX4 level based on Western Blot for unit GPX4 enzymatic activity for comparison. Results were quantified using GraphPad Prism 9.

To measure the effect of small molecules on GPX4 enzymatic activity, 3 μl 10 mM compounds or DMSO control were added to the 96-well plate first, before addition of 147 μL 1.5 μg/μL cell lysate in the GPX4 activity assay buffer and a sequential incubation at 37°C for 20 min. PCOOH was then added to the mixture to initiate GPX4 reaction. GPX4 activity was measured as above.

Cellular viability assay

To monitor the viability of cells without α-tocopherol supplementation, cells that have been cultured in media with without α-tocopherol supplementation were harvested with trypsin, pelleted, and washed with PBS for three times, counted by Vi-cell (Beckman), partially collected for GPX4-specific activity assay, and then equivalently seeded into new cell culture flasks in media without α-tocopherol supplementation on day 1. On every other day (day 3, 5, and 7), cells were harvested with trypsin, counted by Vi-cell, partially collected for GPX4-specific activity assay, before seeding back equivalent number of cells to the corresponding flasks. For quantification, viability was based on the normalization of *viable* cell number of each cell line to the *total* cell number of the corresponding cell line expressing WT GPX4.

For dose response curves, cells were harvested with trypsin, pelleted, and counted by Vi-cell before seeding into plates. 1,000 cells were plated 36 μL per well of a 384-well plate on day 1. For those cell lines which are also subject to the GPX4-specific activity, the remaining cells (after seeding into plates) were immediately tested for Western Blot and activity assay as described above. Compounds were dissolved in DMSO and a two-fold dilution series was prepared. The compounds were then diluted 1:50 in media and 4 μL was added to each well of the plates on day 2. After 48 h of treatment, the viability of cells was measured using 1:1 dilution of the CellTiter-Glo luminescent reagent (Promega G7573) with media, which was read on a Victor 5 plate reader after 10 min of shaking at room temperature on day 4. The intensity of luminescence was normalized to that of DMSO control. Results were quantified using GraphPad Prism 9.

Protein Purification

GPX4 is a selenoprotein with selenocysteine at its active site (U46). Large-scale expression of selenocysteine-containing proteins in recombinant systems is challenging, due to inefficient selenocysteine-incorporating machinery; thus, the selenocysteine to cysteine (U to C, inserting a thiol group in place of the selenol group) mutant of GPX4 is widely used for structural studies, despite its lower enzymatic activity compared to the wild-type protein[32–35]. Since recent studies on selenocysteine-containing GPX4 confirmed the relevance of the catalytic tetrad and other structural properties discovered in the context of the U to C mutant, we used a GPX4[U46C] construct for in vitro structural studies, and simultaneously examined the selenocysteine-containing cytosolic GPX4 in structure-based computational analysis and in human cells via enzymatic assays and cellular assays[11,14,36].

Bacterial expression vector pOE30-His-tagged-c-GPX4[U46C] was described in the previous work[25]. With the vector as template, the following mutagenesis primers were designed using the Agilent QuikChange Primer Design application: R152H (F: 5'- CTG CGT GGT GAA GCA CTA CGG ACC CAT GG –3', R: 5'- CCA TGG GTC CGT AGT GCT TCA CCA CGC AG –3'), K48A (F: 5'- GGC CTC CCA GTG TGG CGC GAC CGA AGT AAA CTA C –3', R: 5'- GTA GTT TAC TTC GGT CGC GCC ACA CTG GGA GGC C –3'), K48L (F: 5'- CGT GGC CTC CCA GTG TGG CCT AAC CGA AGT AAA CTA CAC TC –3', 5'- GAG TGT AGT TTA CTT CGG TTA GGC CAC ACT GGG AGG CCA CG –3'). Primers were purchased from Integrated DNA Technologies. Site-directed mutagenesis kit (QuickChange II, Agilent 200521) was then used to acquire pOE30-c-GPX4[U46C_R152H], pOE30-c-GPX4[U46C_K48A], and pOE30-c-GPX4[U46C_K48L]. All mutations and the resulted plasmids were confirmed by sequencing at GENEWIZ.

Isolated colonies with each plasmid were separately transferred to 8 mL of LB medium with 100 μg/mL ampicillin, and the inoculated culture was incubated while being shaken (225 rpm) at 37 °C for 16 h. 3 mL of the starter culture was added to 1 L of fresh LB medium with 100 μg/mL ampicillin. The culture was incubated while being shaken at 37 °C and 225 rpm until the OD600 reached 0.9. The temperature was then decreased to 15 °C. Cells were incubated with 1 mM isopropyl β-D-1- thiogalactopyranoside (IPTG) while being shaken at 15 °C and 225 rpm overnight. The next day, the bacteria were harvested by centrifugation at 4000g for 20 min at 4 °C and the pellet obtained was ready for purification or stored at −20 °C. The pellet was resuspended in 25 mL of chilled lysis buffer (100 mM Tris pH 8.0, 300 mM NaCl, 20 mM imidazole, 3 mM TCEP, and Roche protease inhibitor cocktail). The bacteria were lysed by sonication on ice for 6 min, and the lysate was centrifuged at 10000 rpm for 20 min at 4 °C to remove cell debris. The clarified lysate was incubated with Ni Sepharose 6 Fast Flow beads (GE Life Sciences) on a rotator at 4 °C for at least 1 h. The beads were washed with wash buffer (100 mM Tris pH 8.0, 300 mM NaCl, 50 mM imidazole, and 3 mM TCEP) to remove nonspecific binding. The protein was eluted with 100 mM Tris pH 8.0, 300 mM NaCl, 100 mM imidazole, and 3 mM TCEP. The protein was further purified using a gel filtration Superdex 200 column in FPLC buffer containing 100 mM Tris pH 8.0, 300 mM NaCl, and 3 mM TCEP. The fractions containing GPX4 were pooled together and analyzed by sodium dodecyl sulfate–polyacrylamide gel electrophoresis (SDS–PAGE).

Crystallization and structure determination

Protein samples of GPX4[U46C] were initially screened at the High-Throughput Crystallization Screening Center[37] of the Hauptman-Woodward Medical Research Institute (HWI) (https://hwi.buffalo.edu/high-throughput-crystallization-center/). The most promising crystal hits were reproduced using under oil micro batch method in a COY anaerobic glove box at 23 °C.

Plate-like crystals of GPX4[U46C] were grown using a crystallization reagent comprising 0.056 M sodium phosphate monobasic monohydrate, pH 8.2 and 1.344 M potassium phosphate with protein to crystallization reagent ratio of 2:1 μl. All crystals were subsequently transferred into a similar crystallization reagent that was supplemented by

20% (v/v) glycerol and flash-frozen in liquid nitrogen in the glove box. A native dataset was collected on a crystal of GPX4[U46C] at the NE-CAT24-ID-C beam line of Advanced Photon Source in Lemont, IL. Crystals of GPX4[U46C] were subsequently used as seeds for growing crystals of GPX4[U46C-R152H], GPX4[U46C-K48L], GPX4[U46C-K48A], and GPX4[U46C]-sulfone outside of the glove box, albeit different crystallization conditions were used for growing these crystals. Crystals of GPX4[U46C-R152H] were grown in a crystallization condition comprising 0.2 M sodium thiocyanate, pH 6.9, and 20% (w/v) PEG 8000, while those of K48L and K48A were grown in a condition consisting of 0.1 M sodium chloride, 0.1 M MES, pH 6, and 40% (w/v) PEG 8000. Crystals of the fully oxidized GPX4[U46C]-sulfone were grown in 0.1 M potassium thiocyanate, 0.1 M sodium acetate, pH 5, and 20% (w/v) PEG 8000, and were harvested after one month. In each case, crystals were transferred into the respective crystallization reagent, which was supplemented by 20% (v/v) ethylene glycol.

Crystals of GPX4[U46C], GPX4[U46C-R152H], GPX4[U46C-K48L], GPX4[U46C-K48A], and GPX4[U46C]-sulfone diffracted X-ray at NE-CAT24-ID-C beam line to resolution 1.38 Å, 1.61 Å, 2.07 Å, 1.52 Å, and 1.48 Å, respectively. The images were respectively processed and scaled in space group $P2_1$, $P2_1$, $P2_1$, $P2_12_12_1$, and $P2_1$, using XDS[38]. The structure of each protein was determined by molecular replacement method using MOLREP[39] program and the crystal structure of GPX4[U46C] (PDB: 2OBI) was used as a search model for structure determination of GPX4[U46C]. The latter structure was used as the search model for subsequent structure determination of other crystal structures. The geometry of each crystal structure was fixed using programs XtalView[40] and COOT[41], and refined by Phenix[42]. There is one protomer of GPX4 in the asymmetric unit (ASU) of the crystal with space group $P2_1$, while the ASU of GPX4-U46C-K48A with space group $P2_12_12_1$ contains two protomers. The crystallographic statistics is shown in Supplementary Table 4.

Thermal Shift Assay (Determination of protein melt temperature)

Since mutation of amino acid residues may alter the thermostability of a protein, we applied thermal shift assay to monitor the potential change in GPX4 thermostability caused by R152H mutation, which practically determined change of the unfolding transition temperature (T_m) obtained on R152H mutant relative to that obtained in the wild type[43,44]. We adapted the assay on fast 96-well PCR plate. *In vitro* purified GPX4[U46C] or GPX4[U46C-R152H] protein was diluted to 5 μM in 20 μL FPLC buffer (100mM Tris pH 8.0, 300 mM NaCl, 3mM TCEP) in each well of a 96-well plate with 5x Sypro orange protein dye, which will bind to the hydrophobic patch of protein once the protein is melted and then exhibit a stronger fluorescence signal. Multiple replicates were prepared for each variant of protein. The thermal shift assay was performed on the ViiA 7 Real-Time PCR system (Thermo Fisher) with the thermal protocol: 25° for 15s, Increase temp to 99° at a rate of 0.05°/sec, 99° for 15 sec. The fluorescence was recorded and analyzed by Protein Thermal Shift™ software.

Immunofluorescence Study and Quantification

Human fibroblast cells RAG01 and RAG02 were separately seeded on poly-lysine-coated coverslips (Sigma Aldrich P4832) in a 24-well plate (100,000 per coverslip and three

coverslips for each cell line) and allowed to grow overnight. Medium was removed and the cells were gently washed with PBS^{2+} (PBS with 1 mM $CaCl_2$ and 0.5 mM $MgCl_2$) gently twice. The cells were fixed and permeabilized by adding 200 μL/well of 4% paraformaldehyde (PFA) in PBS with 0.1% Triton X-100 (PBS-T), and incubated at room temperature for 20 min. The cells were then washed with PBS-T three times. Then the cells were blocked with 5% goat serum (ThermoFisher 50197Z) in PBS-T for 1 h at room temperature. The cells were then incubated with monoclonal mouse GPX4 antibody (Santa Cruz, sc-166570, 1:500 dilution) in PBS-T with 1% BSA and 5% goat serum overnight at 4°C. The cells were washed with PBT for 5 min three times. The cells were incubated with goat anti-mouse IgG (H+L) Highly Cross-Adsorbed Secondary Antibody, Alexa Fluor 594 (Thermo Fisher Scientific Cat# A-11032, RRID:AB_2534091, 1:200 dilution) at room temperature for 1 h. The cells were washed with PBS-T for 5 min three times. ProLong Diamond anti-fade mountant with DAPI (ThermoFisher P36962) was added to stain the nucleus. All images were captured on a Zeiss LSM 800 confocal microscope at Plan-Apochromat 63x/1.40 oil DIC objective with constant laser intensity for all samples.

The quantification of the intensity of antibodies was analyzed using CellProfiler 3.1.8[45] (CellProfiler Image Analysis Software, RRID:SCR_007358). Nuclei were first identified as primary objects using global minimum cross entropy strategy, based on DAPI fluorescence signal. The whole cells were then identified as secondary objects based on primary objects by propagation using global minimum cross entropy strategy, based on GPX4 fluorescence (Alexa Fluor 594) signal. The cytoplasm were then identified as the tertiary objects as the part of each cell excluding the nucleus. Then mean intensities of GPX4 fluorescence of nuclei, cytoplasm and whole cell were measured and reported. Graphs were created in GraphPad Prism 9.

Statistical Analyses

All replicate experiments, unless otherwise indicated, are biological replicates based on distinct samples. All statistical analyses were performed using GraphPad Prism 9. Tukey's test was performed as a post-hoc test after ordinary one-way ANOVA, comparing all pairwise datasets, with alpha = 0.05. Sidak's test was performed as a post-hoc test after ordinary two-way ANOVA for grouped data, comparing pairwise datasets in each group. Only relevant pairwise comparisons are highlighted in the figures. Unpaired Student's t-test was performed when indicated in the manuscript, for comparing two experimental conditions. All t-tests were two tailed and set with a significance threshold of $p < 0.05$.

Data availability

Crystal structural coordinates were deposited in the RCSB, with accession codes PDB IDs: 7L8K, 7L8L, 7L8M, 7L8R, and 7L8Q. Publicly available datasets used in this study are: PDB IDs: 2OBI, 6HN3. Source data are provided with this paper.
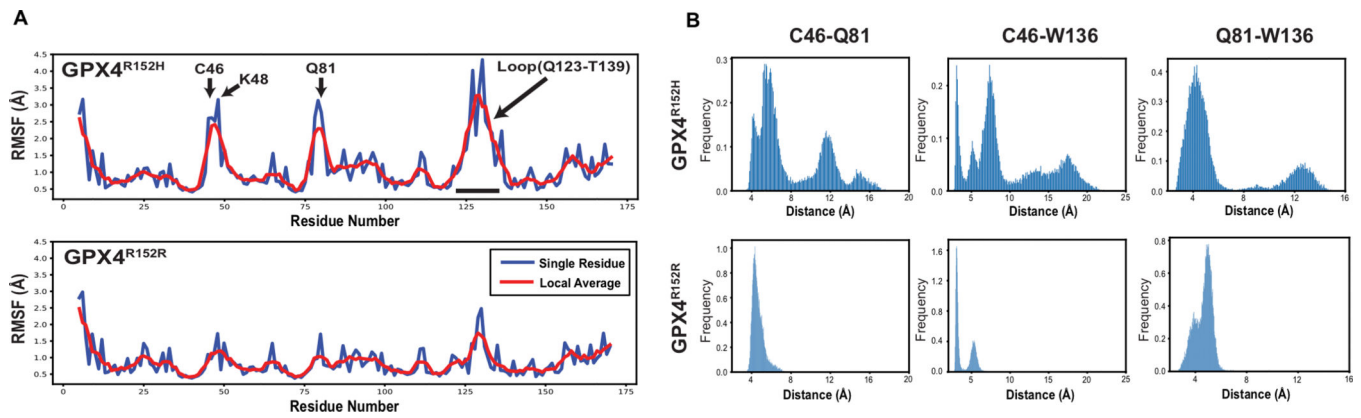
Extended Data
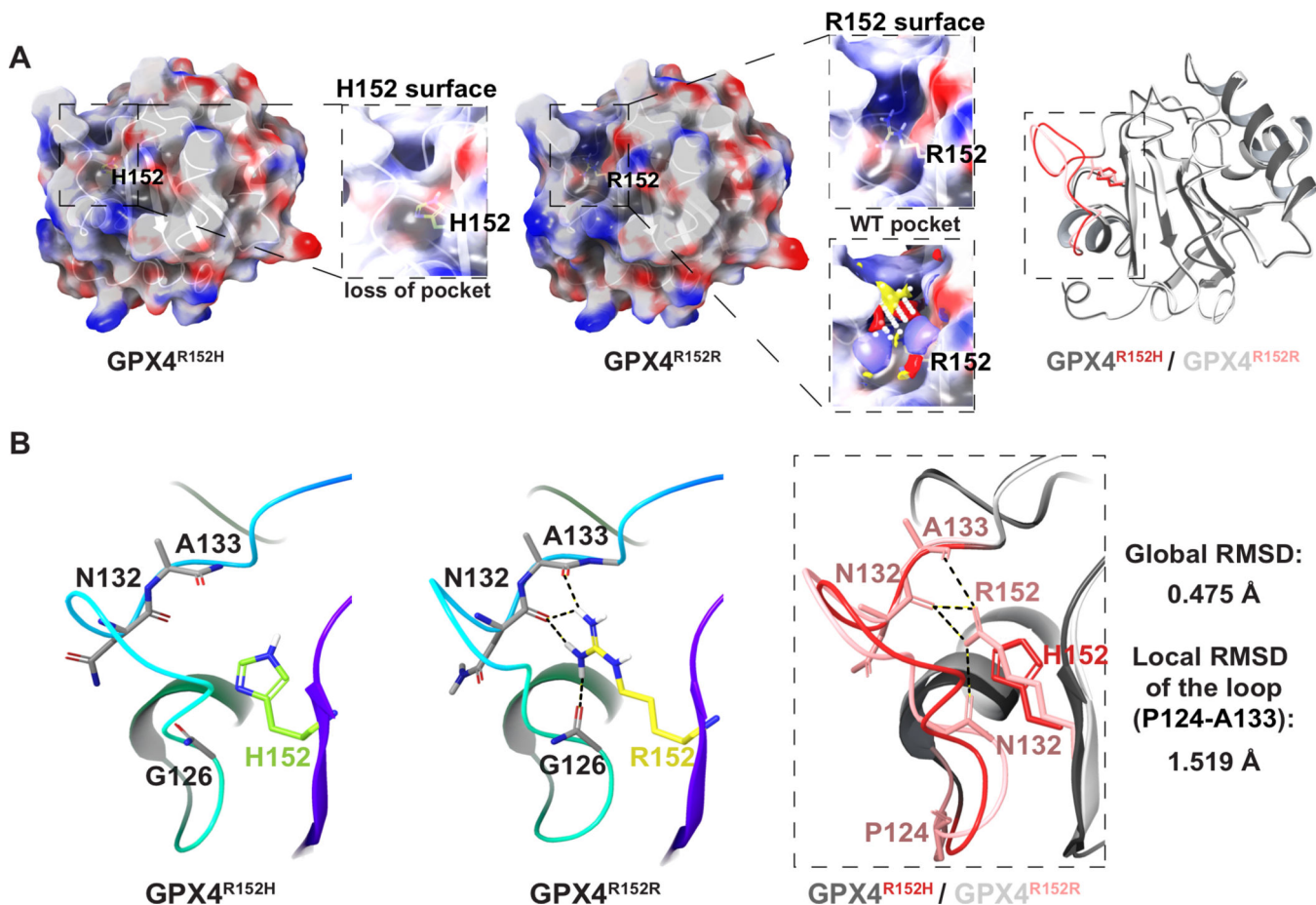
Extended Data Fig. 1. *In silico* **analysis of the impact of R152H mutation on GPX4 (GPX4^{U46C} PDB: 2OBI) structure.**

a, Structure of GPX4^{R152H} was computationally modeled based on the crystal structure of GPX4^{U46C} (PDB: 2OBI). As a control, structure of GPX4^{R152R} was also computationally modeled using the same algorithm, which indeed represents WT GPX4 but excludes artifacts from computational process when compared with the modeled R152H protein structure. Technically the two modeled proteins are GPX4$^{U46C-R152H}$ and GPX4^{U46C}. Protein surface are colored as below: hydrophobic (white), positive charge (red), and negative charge (blue). To visualize the pocket on top of R152 in the GPX4^{R152R} structure, white dots were shown as indicator of space. Overlap of the R152H variant backbone with wild-type was performed in the panel on the right, where the major conformational change in the loop around His152 was colored (WT as in pale pink and R152H as in red). See supplementary note for rationale of using U46C GPX4.

b, The alternation of surface mainly derived from an outstanding conformational change of the loop between Pro124 and Ala133, with which the side chains of Arg152 formed multiple hydrogen bonds in the wild-type, but not His152 in the mutant.

Extended Data Fig. 2. Molecular Dynamic (MD) simulation analysis of the impact of R152H mutation on GPX4.

a, RMSF of each residue in MD simulation based on the modeled GPX4 structure. Representative data from 5 times 100 ns trajectories were plotted.

b, Distances between Cys46 and its catalytic partners Gln81/Trp136 were monitored in the MD simulation of GPX4^{R152H}, as compared to GPX4^{R152R}. Representative data from 5 times 100ns trajectories were plotted.
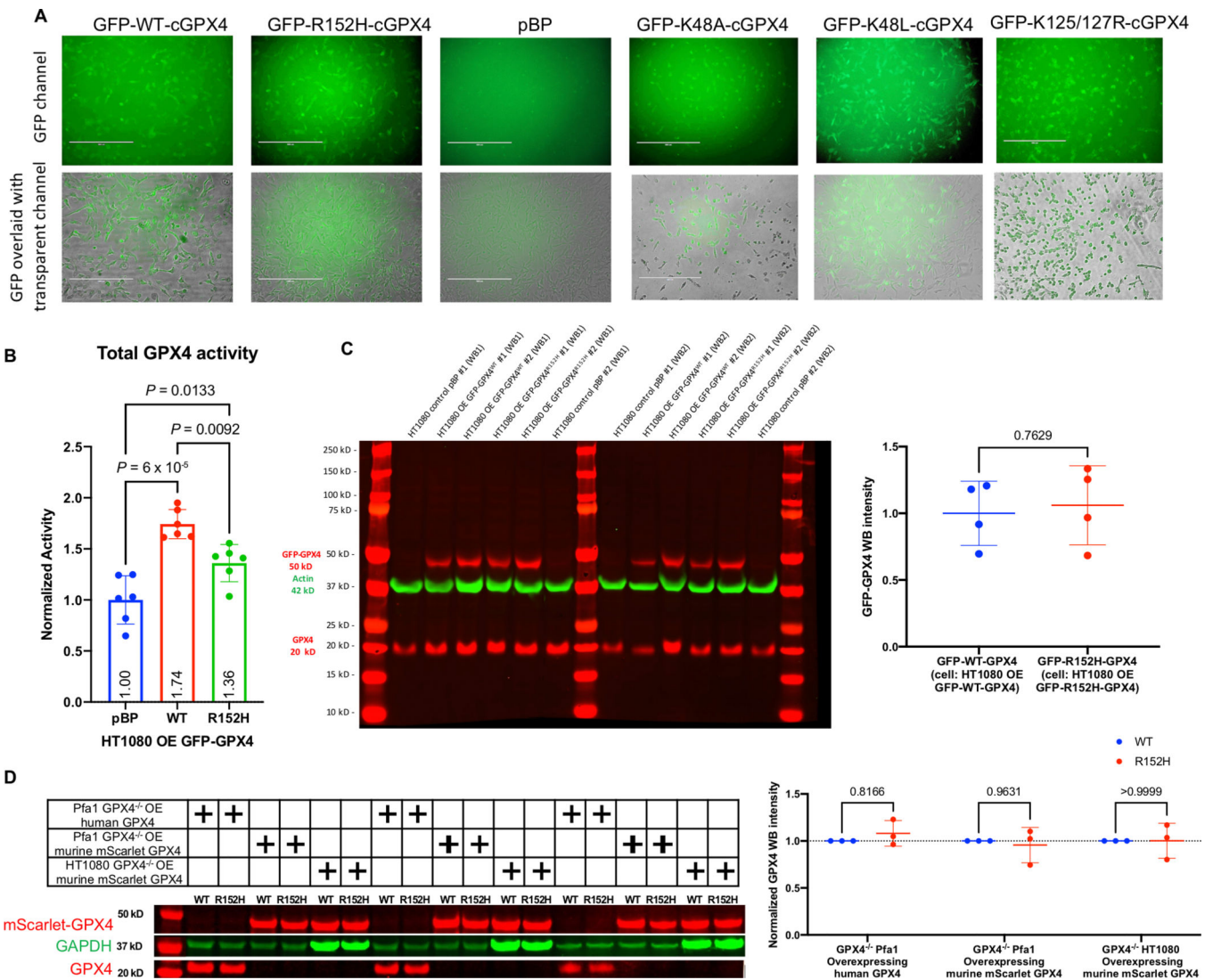
Extended Data Fig. 3. Preparation of cell models of GPX4^R152H.

a, HT1080 transfected with pBP GFP-cGPX4^WT, pBP GFP-cGPX4^R152H, pBabepuro (pBP) empty vector, pBP GFP-cGPX4^K48A, pBP GFP-cGPX4^K48L and pBP GFP-cGPX4^K125R-K127R were selected with puromycin and imaged with microscope. Triplicate experiments were repeated independently with similar results while the representative images were shown. The plotted scale bar is 400 µm.

b, Total GPX4 enzymatic activity (endogenous apo-GPX4 and transfected exogenous GFP-tagged-GPX4) of control HT1080 (pBP, no expression of GFP-tagged-GPX4) and HT1080 cells overexpressing GFP-GPX4^WT or GFP-GPX4^R152H. Data are plotted as means ± SD of six replicate experiments. Ordinary one-way ANOVA followed by Tukey's multiple comparisons test was performed: n=6, DF=15 and P values were plotted.

c, Western blot of control HT1080 (pBP) and HT1080 cells overexpressing GFP-GPX4^WT or GFP-GPX4^R152H using GPX4 and GAPDH antibodies. Expression levels of GFP-WT-GPX4 and GFP-R152H-GPX4 were quantified. Data are plotted as means ± SD, n=4

biologically independent samples. Unpaired two-tailed t test was then performed and plotted: t=0.3158, df=6, P^{ns}=0.7629.

d, Western blot of Gpx4-knockout Pfa1 cells overexpressing exogenous human WT or R152H GPX4, Gpx4-knockout Pfa1 cells overexpressing exogenous murine WT or R152H mScarlet-tagged GPX4, and Gpx4-knockout HT1080 cells overexpressing exogenous murine WT or R152H mScarlet-tagged GPX4 using GPX4 and GAPDH antibodies. Expression levels of GPX4 were quantified. Data are plotted as means ± SD, n=3 biologically independent samples. Ordinary two-way ANOVA followed by Sidak's multiple comparisons test was performed and P values were plotted: n=3, DF=12. Full scan image is shown in the supplemental information.
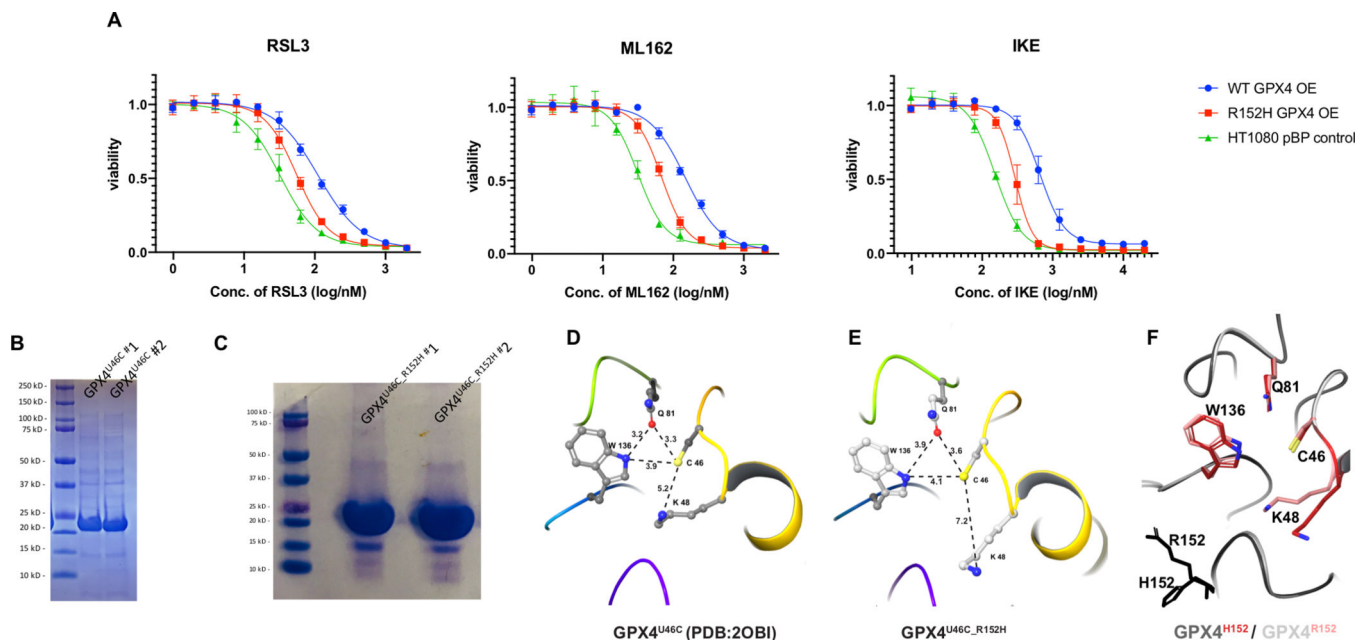
Extended Data Fig. 4. Characterization of GPX4^{R152H} in cells and *in vitro*.

a, HT1080 overexpressing exogenous WT or R152H GFP-GPX4 and a control line were tested for RSL3, ML162, and IKE sensitivity. Data are plotted as means ± SD, n=3 biologically independent samples.

b-c, SDS-PAGE gel of His-tagged GPX4^{U46C} and GPX4$^{U46C\_R152H}$ as stained by Coomasie Blue. Biologically independent duplicate experiments were performed and imaged.

d-e, Distances between the catalytic triad in R152H variant were measured and labeled as compared to GPX4^{U46C} (PDB:2OBI).

f, Shift of Lys48 away from the active site in the GPX4^{R152H} was plotted.
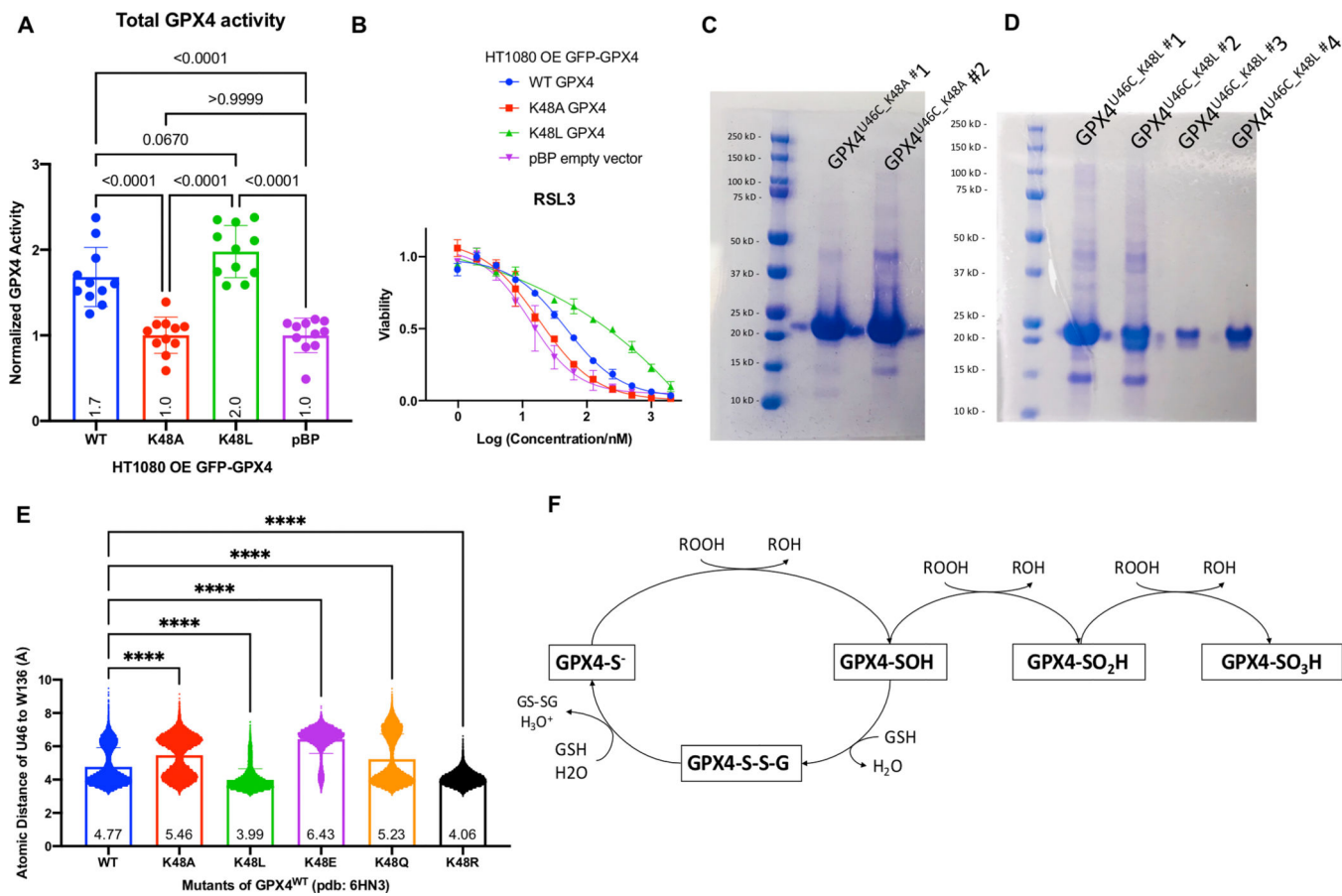
Extended Data Fig. 5. Characterization of Lysine 48 mutants of GPX4 *in cells* and *in vitro*.
**a,** Total GPX4 activity of HT1080 cells overexpressing GFP-GPX4^{WT}, GFP-GPX4^{K48A}, or GFP-GPX4^{K48L} and a control line. Data are plotted as means ± SD of eleven biologically independent replicate experiments. Ordinary one-way ANOVA followed by Tukey's multiple comparisons test was performed and P values were plotted, n=11, DF=40.
b, HT1080 overexpressing exogenous WT, K48A, or K48L GFP-GPX4 and a control line were tested for RSL3 sensitivity. Data are plotted as means ± SD of three biologically independent replicate experiments.
c-d, SDS-PAGE gel of His-tagged GPX4$^{U46C\_K48A}$ and GPX4$^{U46C\_K48L}$ as stained by Coomasie Blue. Biologically independent duplicate (GPX4$^{U46C\_K48A}$) and quadruplicate (GPX4$^{U46C\_K48L}$) experiments were performed and imaged.
e, The distances between catalytic residues Sec46 and Trp136 were recorded every 4.8 ps throughout MD simulations of GPX4^{WT} (PDB: 6HN3), GPX4^{K48A}, GPX4^{K48L}, GPX4^{K48E}, GPX4^{K48Q}, and GPX4^{K48R}. Representative data from three times 100 ns trajectories were plotted as means ± SD. Ordinary one-way ANOVA followed by Tukey's multiple comparisons test was performed: n=20835, DF=125004, all P****<1×10^{-20}.
f, Scheme illustrating the catalytic cycle of sulfur-containing variant of GPX4.
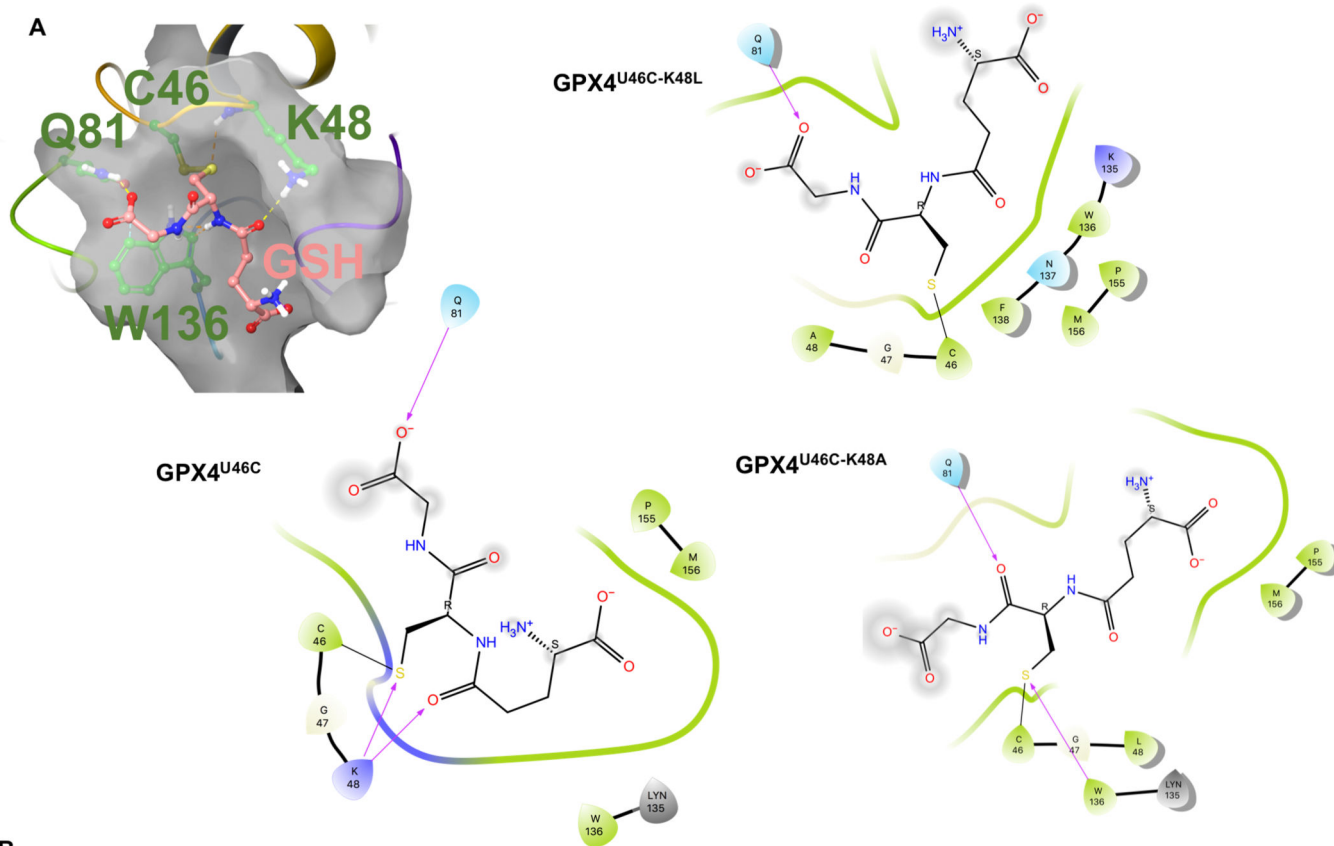
Extended Data Fig. 6. Characterization of Lysine 48 mutants of GPX4 *in silico*.
a, In silico docking of GSH to GPX4^U46C, GPX4^K48A, or GPX4^K48L. Top covalent-docking pose of GSH on GPX4^U46C (top left). 2D Ligand interaction diagram of GSH with GPX4^U46C, GPX4^K48A, or GPX4^K48L in their individually top covalent-docking pose (top right and bottom panels).
b, HT1080 overexpressing exogenous WT, K48A, or K48L GFP-GPX4 and a control line were tested for IKE sensitivity. Data are plotted as means ± SD of three biologically independent replicate experiments.
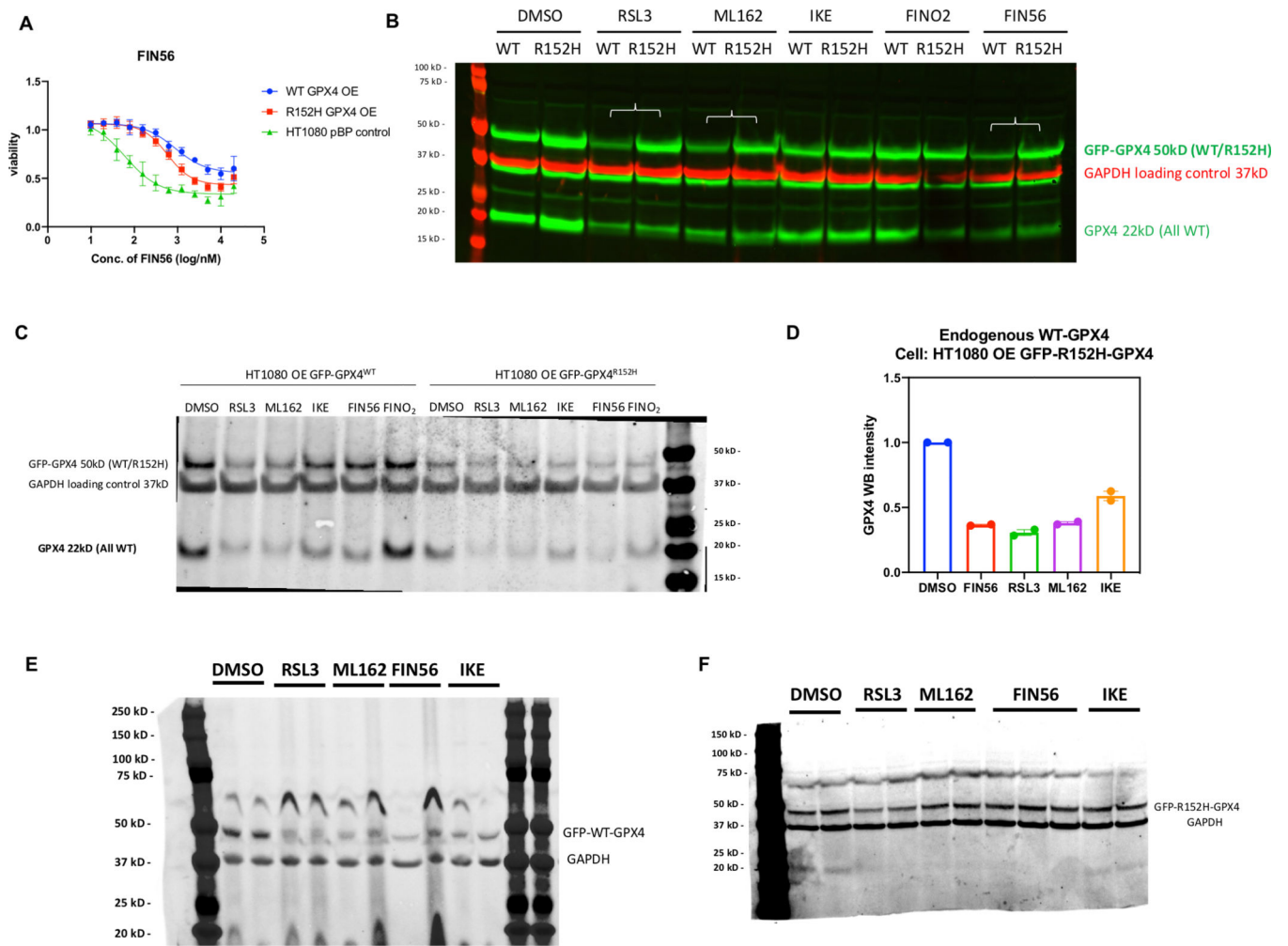
Extended Data Fig. 7. Investigation of GPX4 degradation mechanism after treatment with ferroptosis inducers.

a, HT1080 overexpressing exogenous WT or R152H GFP-GPX4 and a control line were tested for FIN56 sensitivity. Data are plotted as means ± SD, n=3 biologically independent samples.

b, Western blot of HT1080 OE GFP-GPX4^{WT} and HT1080 OE GFP-GPX4^{R152H} after treatment with ferroptosis inducers with GPX4 and GAPDH antibodies, with lanes arranged for cell line comparison. Triplicate experiments were repeated independently with similar results, which were shown in Extended Data Figure 7c, 7e, and 7f.

c, Western blot of HT1080 OE GFP-GPX4^{WT} and HT1080 OE GFP-GPX4^{R152H} after treatment with ferroptosis inducers with GPX4 and GAPDH antibodies, with lanes arranged for ferroptosis inducer comparison. Triplicate experiments were repeated independently with similar results, which were shown in Extended Data Figure 7b, 7e, and 7f.

d, The endogenous GPX4 in HT1080 OE GFP-R152H-GPX4 were tested for vulnerability to the degradation induced by RSL3, ML162, FIN56, and IKE. Data are plotted as means with range of two biologically independent experiments. The corresponding blots are shown in Extended Data Figure 7b and 7c.

e, Western blot of HT1080 OE GFP-GPX4^{WT} after treatment with ferroptosis inducers with GPX4 and GAPDH antibodies. Triplicate experiments were repeated independently with similar results, which were shown in Extended Data Figure 7b and 7c.

f, Western blot of HT1080 OE GFP-GPX4^{R152H} after treatment with ferroptosis inducers using GPX4 and GAPDH antibodies. Triplicate experiments were repeated independently with similar results, which were shown in Extended Data Figure 7b and 7c.
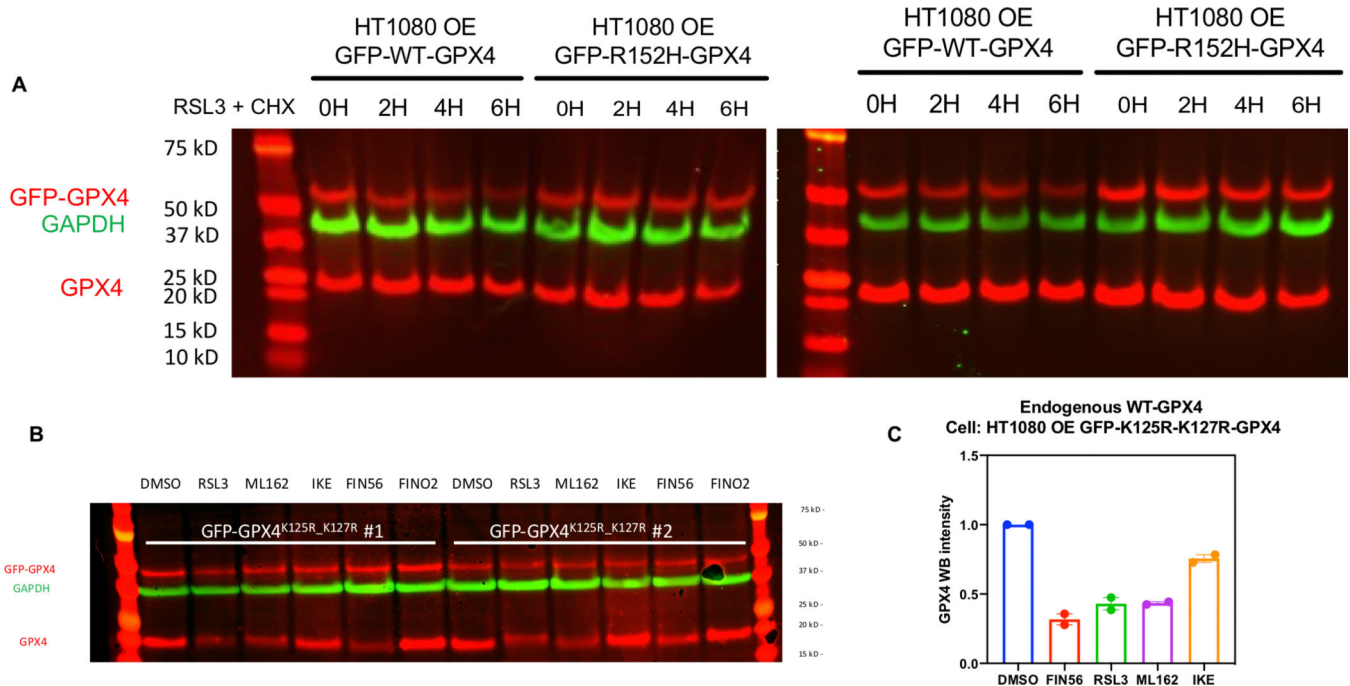
Extended Data Fig. 8. Kinetic and mutagenesis study of GPX4 degradation mechanism after treatment with ferroptosis inducers.
a, HT1080 OE GFP-GPX4^{WT} and HT1080 OE GFP-GPX4^{R152H} were treated with 4 μM RSL3, 30 μg/ml cycloheximide, and 100 μM a-Tocopherol for 0, 2, 4, or 6 hours before Western Blot analysis of GPX4 and GADPH. Biologically independent duplicate experiments were performed and imaged.
b, Western blot of HT1080 OE GPX4$^{K125R\_K127R}$ after treatments with ferroptosis inducers using GPX4 and GAPDH antibodies. Duplicate experiments were performed and imaged.
**c,** The endogenous GPX4 in HT1080 OE GFP-K125R-K127R-GPX4 were tested for vulnerability to the degradation induced by RSL3, ML162, FIN56, and IKE. Data are plotted as means with range of two biologically independent experiments. The corresponding blots are shown in Extended Data Figure 8b.
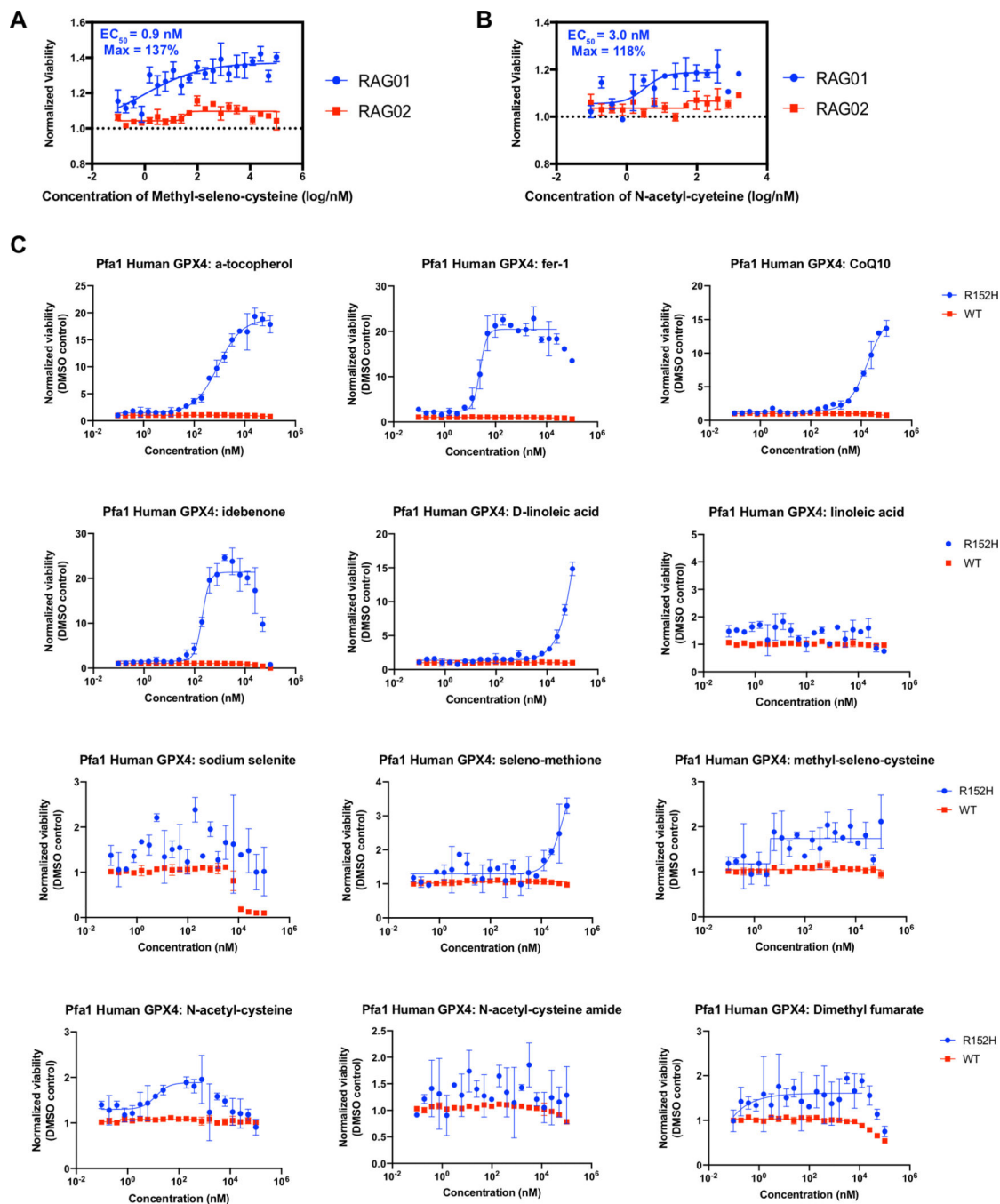
Extended Data Fig. 9. Proof-of-concept treatments were tested on patient fibroblasts and Pfa1 cells, which were knocked out of endogenous GPX4 and transfected to overexpress human mScarlet-tagged GPX4^{WT} (red) or GPX4^{R152H} (blue).

a-b, Supplementations of methylseleno-cysteine and N-acetyl-cysteine were tested as proof-of-concept treatments on the patient and control fibroblasts. Data are plotted as means ± SD (n=3 biologically independent samples).

c, Viability was normalized to the corresponding DMSO control. Data are plotted as means ± SD (n=3 biologically independent samples). See supplementary note for effects of α-tocopherol.
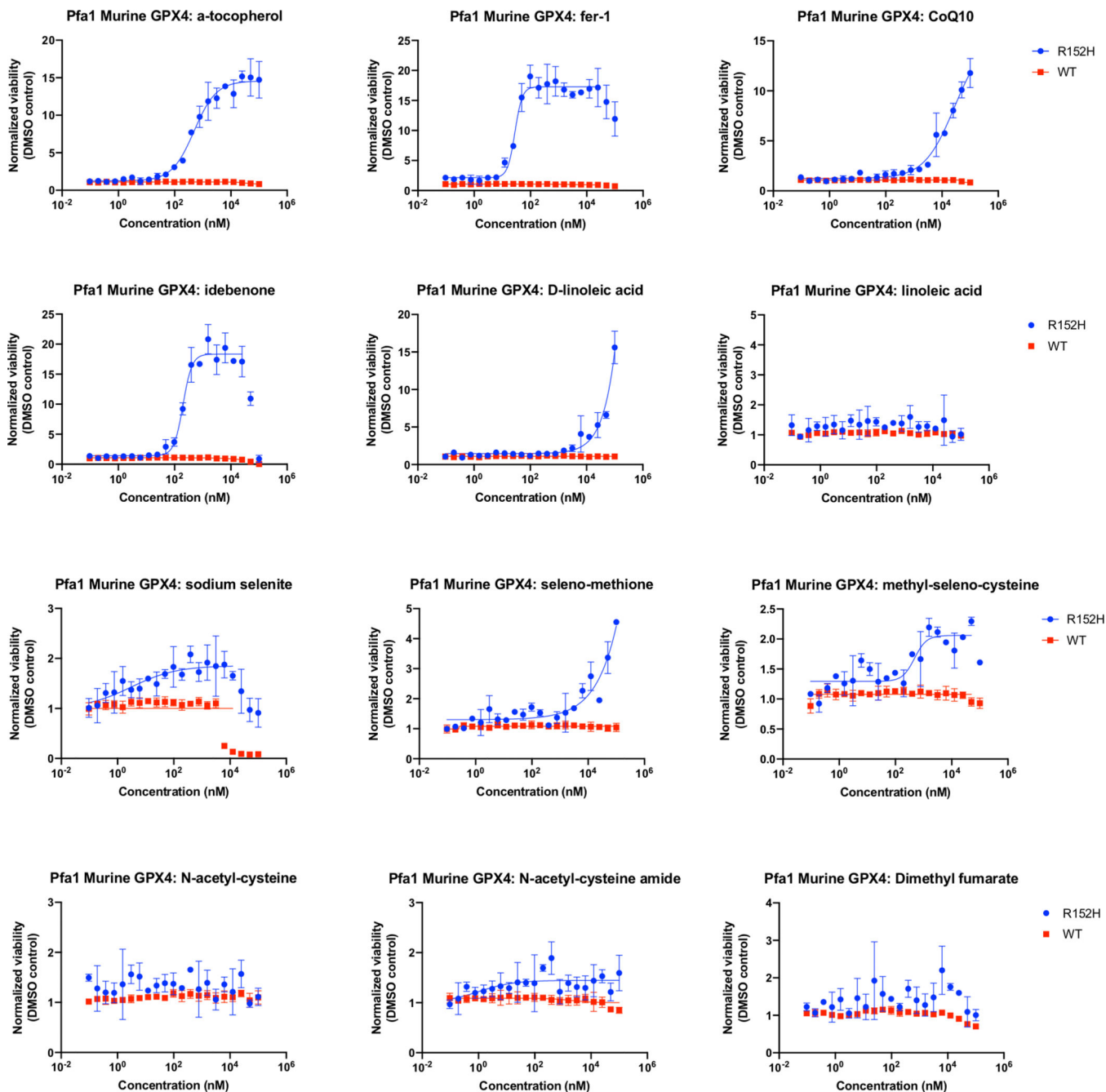
Extended Data Fig. 10. Proof-of-concept treatments were validated in Pfa1 cells, which were knocked out of endogenous GPX4 and transfected to overexpress murine mScarlet-tagged GPX4WT (red) or GPX4R152H (blue).
Viability was normalized to the corresponding DMSO control. Data are plotted as means ± SD (n=3 biologically independent samples). See supplementary note for effects of α-tocopherol.

Supplementary Material

Refer to Web version on PubMed Central for supplementary material.

Acknowledgements

Declaration of Interests

BRS is an inventor on patents and patent applications related to GPX4 and ferroptosis, and is a consultant to and co-founder of Inzen Therapeutics and Nevrox Limited, and is a member of the Scientific Advisory Board of Weatherwax Biotechnologies Corporation, and a consultant to Akin Gump Strauss Hauer & Feld LLP. MC is an inventor of ferroptosis-related patents and co-founder and shareholder of ROSCUE Therapeutics GmbH. JF participates in Clinical Trials with Biogen (Angelman's Syndrome) and JF's spouse is Founder and Principal of Friedman Bioventure, which holds a variety of publicly traded and private biotechnology interests

References

1. Elcioglu N. & Hall CM Spondylometaphyseal dysplasia-Sedaghatian type. Am J Med Genet 76, 410–414 (1998). [PubMed: 9556300]

2. pek MS & Akin A. Sedaghatian-Type Spondylometaphyseal Dysplasia: A Case of Rapid Demise with Evidence of Myocardial Injury. J Genet Genome Res 3, 25–27, doi:10.23937/2378-3648/1410025 (2016).

3. Smith AC et al. Mutations in the enzyme glutathione peroxidase 4 cause Sedaghatian-type spondylometaphyseal dysplasia. J Med Genet 51, 470–474, doi:10.1136/jmedgenet-2013-102218 (2014). [PubMed: 24706940]

4. Fedida A. et al. Sedaghatian-type spondylometaphyseal dysplasia: Whole exome sequencing in neonatal dry blood spots enabled identification of a novel variant in GPX4. Eur J Med Genet 63, 104020, doi:10.1016/j.ejmg.2020.104020 (2020). [PubMed: 32827718]

5. Brigelius-Flohe R. & Maiorino M. Glutathione peroxidases. Biochim Biophys Acta 1830, 3289–3303, doi:10.1016/j.bbagen.2012.11.020 (2013). [PubMed: 23201771]

6. Yang WS et al. Regulation of ferroptotic cancer cell death by GPX4. Cell 156, 317–331, doi:10.1016/j.cell.2013.12.010 (2014). [PubMed: 24439385]

7. Seiler A. et al. Glutathione peroxidase 4 senses and translates oxidative stress into 12/15-lipoxygenase dependent- and AIF-mediated cell death. Cell Metab 8, 237–248, doi:10.1016/j.cmet.2008.07.005 (2008). [PubMed: 18762024]

8. Yant LJ et al. The selenoprotein GPX4 is essential for mouse development and protects from radiation and oxidative damage insults. Free Radic Biol Med 34, 496–502, doi:10.1016/s0891-5849(02)01360-6 (2003). [PubMed: 12566075]

9. Tosatto SC et al. The catalytic site of glutathione peroxidases. Antioxid Redox Signal 10, 1515–1526, doi:10.1089/ars.2008.2055 (2008). [PubMed: 18500926]

10. Roveri A, Maiorino M. & Ursini F. Enzymatic and immunological measurements of soluble and membrane-bound phospholipid-hydroperoxide glutathione peroxidase. Methods Enzymol 233, 202–212, doi:10.1016/s0076-6879(94)33023-9 (1994). [PubMed: 8015457]

11. Ingold I. et al. Selenium Utilization by GPX4 Is Required to Prevent Hydroperoxide-Induced Ferroptosis. Cell 172, 409–422 e421, doi:10.1016/j.cell.2017.11.048 (2018). [PubMed: 29290465]

12. Ingold I. et al. Expression of a Catalytically Inactive Mutant Form of Glutathione Peroxidase 4 (Gpx4) Confers a Dominant-negative Effect in Male Fertility. J Biol Chem 290, 14668–14678, doi:10.1074/jbc.M115.656363 (2015). [PubMed: 25922076]

13. Mannes AM, Seiler A, Bosello V, Maiorino M. & Conrad M. Cysteine mutant of mammalian GPx4 rescues cell death induced by disruption of the wild-type selenoenzyme. FASEB J 25, 2135–2144, doi:10.1096/fj.10-177147 (2011). [PubMed: 21402720]

14. Borchert A. et al. Crystal structure and functional characterization of selenocysteine-containing glutathione peroxidase 4 suggests an alternative mechanism of peroxide reduction. Biochim Biophys Acta Mol Cell Biol Lipids 1863, 1095–1107, doi:10.1016/j.bbalip.2018.06.006 (2018). [PubMed: 29883798]

15. Zhu K. et al. Docking covalent inhibitors: a parameter free approach to pose prediction and scoring. J Chem Inf Model 54, 1932–1940, doi:10.1021/ci500118s (2014). [PubMed: 24916536]

16. Mauri P. et al. Versatility of selenium catalysis in PHGPx unraveled by LC/ESI-MS/MS. Biol Chem 384, 575–588, doi:10.1515/BC.2003.065 (2003). [PubMed: 12751787]

17. Shimada K. et al. Global survey of cell death mechanisms reveals metabolic regulation of ferroptosis. Nat Chem Biol 12, 497–503, doi:10.1038/nchembio.2079 (2016). [PubMed: 27159577]

18. Gaschler MM et al. FINO2 initiates ferroptosis through GPX4 inactivation and iron oxidation. Nat Chem Biol 14, 507–515, doi:10.1038/s41589-018-0031-6 (2018). [PubMed: 29610484]

19. Wu Z. et al. Chaperone-mediated autophagy is involved in the execution of ferroptosis. Proc Natl Acad Sci U S A 116, 2996–3005, doi:10.1073/pnas.1819728116 (2019). [PubMed: 30718432]

20. Romanowska M. et al. Effects of selenium supplementation on expression of glutathione peroxidase isoforms in cultured human lung adenocarcinoma cell lines. Lung Cancer 55, 35–42, doi:10.1016/j.lungcan.2006.09.007 (2007). [PubMed: 17052796]

21. Bodnar M, Szczyglowska M, Konieczka P. & Namiesnik J. Methods of Selenium Supplementation: Bioavailability and Determination of Selenium Compounds. Crit Rev Food Sci Nutr 56, 36–55, doi:10.1080/10408398.2012.709550 (2016). [PubMed: 24987868]

22. Yang WS & Stockwell BR Ferroptosis: Death by Lipid Peroxidation. Trends Cell Biol 26, 165–176, doi:10.1016/j.tcb.2015.10.014 (2016). [PubMed: 26653790]

23. Wang Q. et al. Dimethyl Fumarate Protects Neural Stem/Progenitor Cells and Neurons from Oxidative Damage through Nrf2-ERK1/2 MAPK Pathway. Int J Mol Sci 16, 13885–13907, doi:10.3390/ijms160613885 (2015). [PubMed: 26090715]

24. Hatami A. et al. Deuterium-reinforced linoleic acid lowers lipid peroxidation and mitigates cognitive impairment in the Q140 knock in mouse model of Huntington's disease. FEBS J 285, 3002–3012, doi:10.1111/febs.14590 (2018). [PubMed: 29933522]

25. Yang WS et al. Peroxidation of polyunsaturated fatty acids by lipoxygenases drives ferroptosis. Proc Natl Acad Sci U S A 113, E4966–4975, doi:10.1073/pnas.1603244113 (2016). [PubMed: 27506793]

26. Brenna JT et al. Plasma and Red Blood Cell Membrane Accretion and Pharmacokinetics of RT001 (bis-Allylic 11,11-D2-Linoleic Acid Ethyl Ester) during Long Term Dosing in Patients. J Pharm Sci 109, 3496–3503, doi:10.1016/j.xphs.2020.08.019 (2020). [PubMed: 32871154]

27. Yoo SE et al. Gpx4 ablation in adult mice results in a lethal phenotype accompanied by neuronal loss in brain. Free Radic Biol Med 52, 1820–1827, doi:10.1016/j.freeradbiomed.2012.02.043 (2012). [PubMed: 22401858]

28. Wirth EK et al. Neuronal selenoprotein expression is required for interneuron development and prevents seizures and neurodegeneration. FASEB J 24, 844–852, doi:10.1096/fj.09-143974 (2010). [PubMed: 19890015]

29. Hangauer MJ et al. Drug-tolerant persister cancer cells are vulnerable to GPX4 inhibition. Nature 551, 247–250, doi:10.1038/nature24297 (2017). [PubMed: 29088702]

30. Liu H, Schreiber SL & Stockwell BR Targeting Dependency on the GPX4 Lipid Peroxide Repair Pathway for Cancer Therapy. Biochemistry 57, 2059–2060, doi:10.1021/acs.biochem.8b00307 (2018). [PubMed: 29584411]

31. Viswanathan VS et al. Dependency of a therapy-resistant state of cancer cells on a lipid peroxidase pathway. Nature 547, 453–457, doi:10.1038/nature23007 (2017). [PubMed: 28678785]

Reference list for Methods section

32. Janowski R, Scanu S, Niessing D. & Madl T. Crystal and solution structural studies of mouse phospholipid hydroperoxide glutathione peroxidase 4. Acta Crystallogr F Struct Biol Commun 72, 743–749, doi:10.1107/S2053230X16013686 (2016). [PubMed: 27710939]

33. Li C. et al. Novel Allosteric Activators for Ferroptosis Regulator Glutathione Peroxidase 4. J Med Chem 62, 266–275, doi:10.1021/acs.jmedchem.8b00315 (2019). [PubMed: 29688708]

34. Sakamoto K. et al. Discovery of GPX4 inhibitory peptides from random peptide T7 phage display and subsequent structural analysis. Biochem Biophys Res Commun 482, 195–201, doi:10.1016/j.bbrc.2016.11.035 (2017). [PubMed: 27836545]

35. Scheerer P. et al. Structural basis for catalytic activity and enzyme polymerization of phospholipid hydroperoxide glutathione peroxidase-4 (GPx4). Biochemistry 46, 9041–9049, doi:10.1021/bi700840d (2007). [PubMed: 17630701]

36. Yu Y. et al. Characterization and structural analysis of human selenium-dependent glutathione peroxidase 4 mutant expressed in Escherichia coli. Free Radic Biol Med 71, 332–338, doi:10.1016/j.freeradbiomed.2014.03.032 (2014). [PubMed: 24681209]

37. Luft JR et al. A deliberate approach to screening for initial crystallization conditions of biological macromolecules. J Struct Biol 142, 170–179, doi:10.1016/s1047-8477(03)00048-0 (2003). [PubMed: 12718929]

38. Kabsch W. Integration, scaling, space-group assignment and post-refinement. Acta Crystallogr D Biol Crystallogr 66, 133–144, doi:10.1107/S0907444909047374 (2010). [PubMed: 20124693]

39. Vagin A. & Teplyakov A. Molecular replacement with MOLREP. Acta Crystallogr D Biol Crystallogr 66, 22–25, doi:10.1107/S0907444909042589 (2010). [PubMed: 20057045]

40. McRee DE XtalView/Xfit--A versatile program for manipulating atomic coordinates and electron density. J Struct Biol 125, 156–165, doi:10.1006/jsbi.1999.4094 (1999). [PubMed: 10222271]

41. Emsley P, Lohkamp B, Scott WG & Cowtan K. Features and development of Coot. Acta Crystallogr D Biol Crystallogr 66, 486–501, doi:10.1107/S0907444910007493 (2010). [PubMed: 20383002]

42. Adams PD et al. PHENIX: a comprehensive Python-based system for macromolecular structure solution. Acta Crystallogr D Biol Crystallogr 66, 213–221, doi:10.1107/S0907444909052925 (2010). [PubMed: 20124702]

43. Lo MC et al. Evaluation of fluorescence-based thermal shift assays for hit identification in drug discovery. Anal Biochem 332, 153–159, doi:10.1016/j.ab.2004.04.031 (2004). [PubMed: 15301960]

44. Kaplan A. et al. Small molecule-induced oxidation of protein disulfide isomerase is neuroprotective. Proc Natl Acad Sci U S A 112, E2245–2252, doi:10.1073/pnas.1500439112 (2015). [PubMed: 25848045]

45. Carpenter AE et al. CellProfiler: image analysis software for identifying and quantifying cell phenotypes. Genome Biol 7, R100, doi:10.1186/gb-2006-7-10-r100 (2006). [PubMed: 17076895]
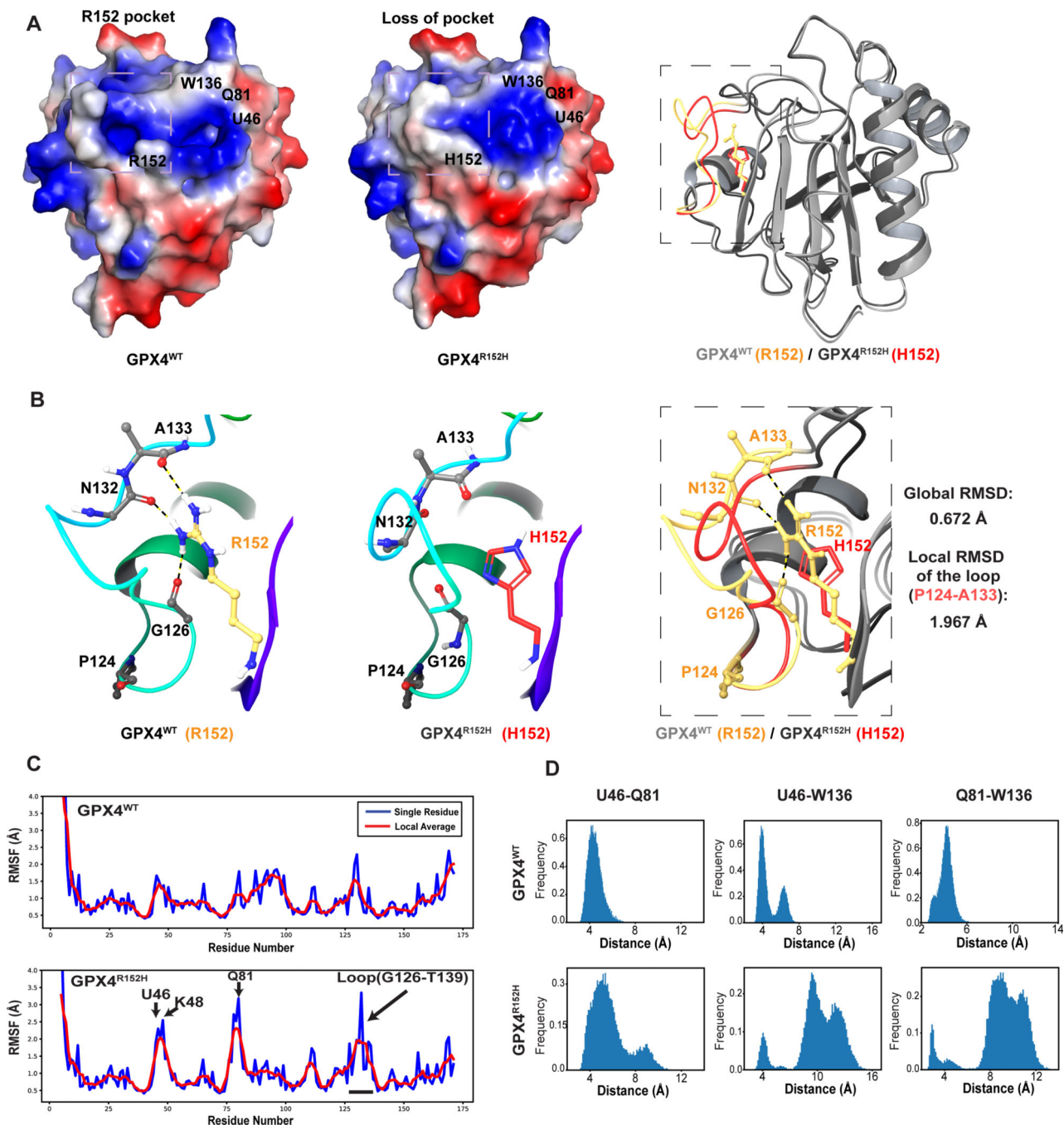
Figure 1. *In silico* **analysis of the impact of R152H mutation on GPX4 structure (GPX4[WT] PDB: 6HN3) predicted significantly conformational change and increased flexibility of local loop and the active site.**

a, Structure of GPX4[R152H] was computationally modeled based on the crystal structure of GPX4[WT] (PDB: 6HN3). Surface potential analysis of both wild-type and R152H variant of GPX4 was conducted. Protein surface are colored as below: hydrophobic (white), positive charge (red), and negative charge (blue). Overlap of the R152H variant backbone with wild-type was performed in the panel on the right, where the major conformational change in the loop around His152 was colored (WT as in yellow and R152H as in red).

b, The alternation of surface mainly derived from an outstanding conformational change of the loop between Pro124 and Ala133, with which the side chains of Arg152 formed multiple hydrogen bonds in the wild-type, but not His152 in the mutant.

c, RMSF of each residue in MD simulations of GPX4^{R152H} and GPX4^{WT}. Representative data from 3 times 100 ns trajectories were plotted.

d, Distances between Sec46 and its catalytic partners Gln81/Trp136 were monitored in the MD simulation of GPX4^{R152H}, as compared to GPX4^{WT}. Representative data from 3 times 100ns trajectories were plotted.
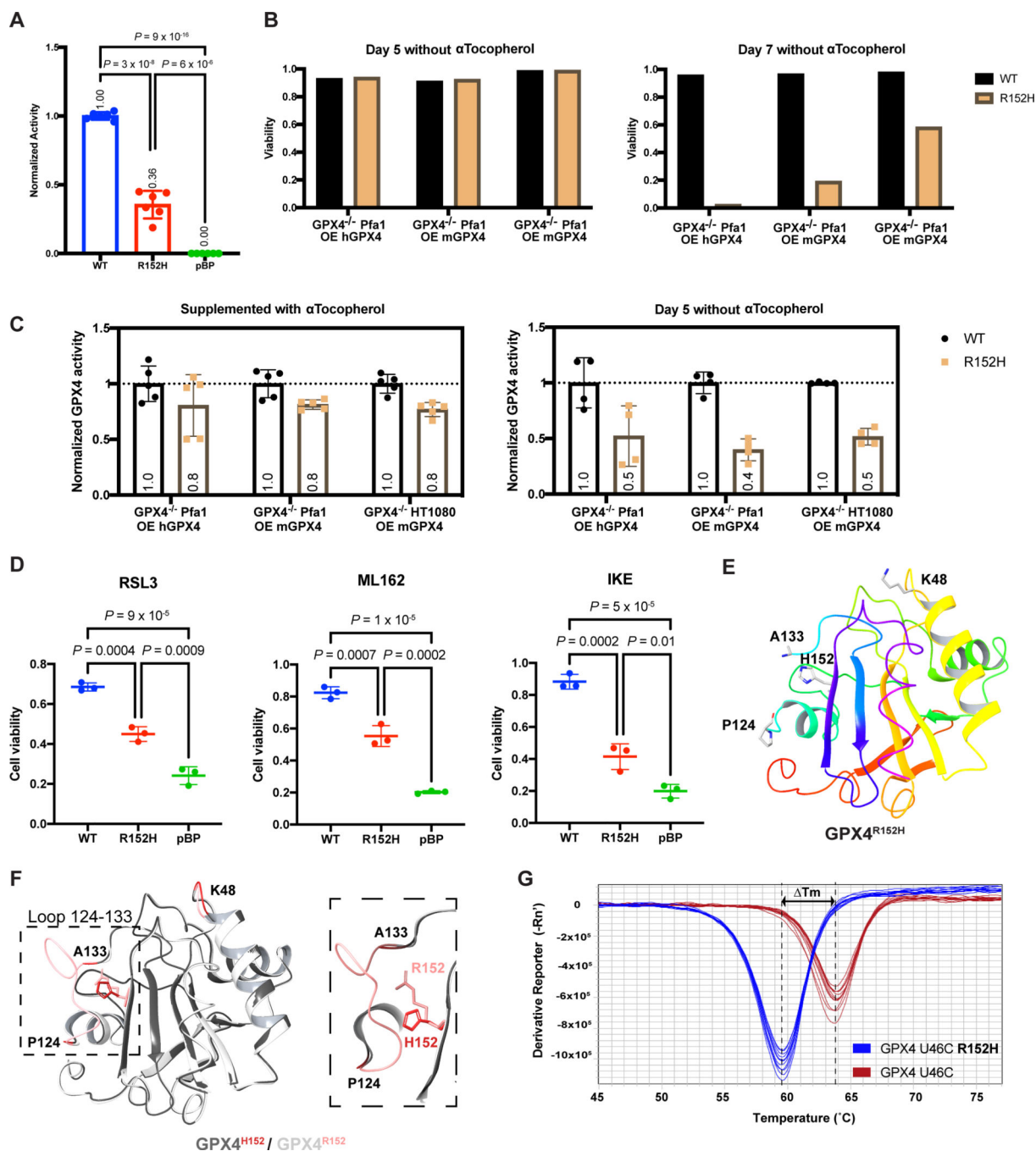
Figure 2. R152H mutation resulted in a partial loss of function and structural change of GPX4.
a, Using HT1080 transfected with pBabe-puro (pBP) empty vector as control, the activity of WT or R152H GFP-tagged cytosolic GPX4 in HT1080 was measured in an NADPH-coupled GPX4 activity assay and then normalized with the WB intensity of GFP-GPX4. Data are plotted as means ± SD of six replicate experiments. Ordinary one-way ANOVA followed by Tukey's multiple comparisons test was performed, n=6, DF=15. P values were plotted.

b, Viabilities of Gpx4-knockout Pfa1 cells overexpressing exogenous human WT or R152H GPX4, Gpx4-knockout Pfa1 cells overexpressing exogenous murine WT or R152H mScarlet-tagged GPX4, and Gpx4-knockout HT1080 cells overexpressing exogenous murine WT or R152H mScarlet-tagged GPX4 were measured on day 5 and day 7 after removal of α-tocopherol from cell media.

c, Activity of GPX4 in Gpx4-knockout cells overexpressing exogenous WT or R152H GPX4 was measured on day 0 and day 5 after removal of α-tocopherol from cell media. Data are plotted as means ± SD, n=5 biologically independent samples for day 0 (left panel), while n=4 biologically independent samples for day 5 (right panel). See methods of cell culture note for discussion on effects of α-tocopherol.

d, Viabilities of HT1080 overexpressing exogenous WT or R152H GFP-GPX4 and a control line were measured after treatment of RSL3 (62.5 nM), ML162 (62.5 nM), and IKE (0.3 μM) for 48 hours. Data are plotted as means ± SD, n=3 biologically independent samples. Two-tailed t tests were then performed and P values were plotted.

e, The crystal structure of GPX4$^{R152H\_U46C}$. Loss of electron density corresponding to the loop indicates the lack of fixed or ordered three-dimensional structure in this part of the protein. See Methods for rationale of using U46C GPX4.

f, Overlap of GPX4$^{R152H\_U46C}$ with the GPX4^{U46C} also revealed a conformational change of Lys48, which is around the active site. The structure of GPX4^{U46C} that we solved is consistent with the previously reported structure (PDB: 2OBI).

g, Melt temperatures of GPX4$^{R152H\_U46C}$ and GPX4^{U46C} were measured in the thermal shift assay with Sypro Orange as reporter (n=12 biologically independent samples).
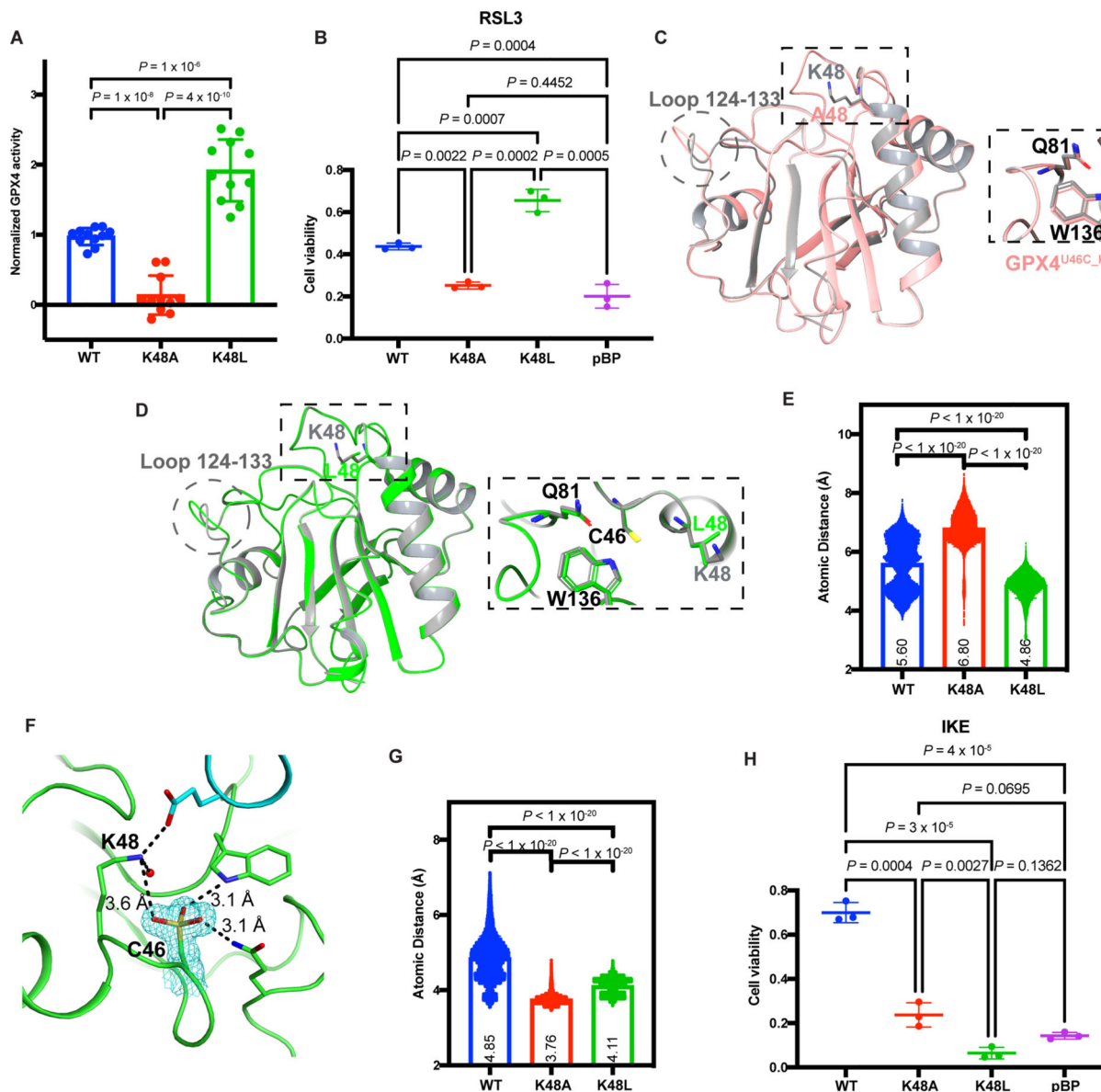
Figure 3. Lys48 modulates the enzymatic function of GPX4.

a, Using HT1080 transfected with pBP empty vector as control, the activities of WT, K48A, and K48L GFP-tagged cytosolic GPX4 in were measured in an NADPH-coupled GPX4 activity assay. Data are plotted as means ± SD of eleven replicate experiments. Ordinary one-way ANOVA followed by Tukey's multiple comparisons test was performed, n=11, DF=30. P values were plotted.

b, Viabilities of HT1080 overexpressing exogenous WT, K48A, or K48L GFP-GPX4 and a control line were measured after treatment of RSL3 (62.5 nM) for 48 hours. Data are plotted as means ± SD, n=3 biologically independent samples. Two-tailed t tests were then performed and P values were plotted.

c, The crystal structure of GPX4$^{U46C\_K48A}$ aligned with that of GPX4^{U46C}.

d, The crystal structure of GPX4$^{U46C\_K48L}$ aligned with that of GPX4^{U46C}.

e, The distances between catalytic residues Cys46 and Trp136 were recorded every 4.8 ps throughout ten independent 100 ns MD simulations of GPX4^{U46C}, GPX4$^{U46C\_K48A}$, and GPX4$^{U46C\_K48L}$. All n=208,350 independent measurements of distances throughout the throughout the ten independent simulations were plotted, with means ± SD. Unpaired two-tailed t test was then performed and P values were plotted.

f, In the crystal structure of oxidized GPX4^{U46C} (Cys46-SO$_3$H), Lys48 is in close proximity to the oxidized Cys46. The F_o-F_c omit map (cyan mesh) contoured at 3 σ. The side chain of E65 (in cyan) belongs to protomer B. The solid red sphere represents a water molecule in the active site.

g, The distances between catalytic residues Cys46 and Trp136 were recorded every 4.8 ps throughout five times 100 ns MD simulations of oxidized GPX4^{U46C}, GPX4$^{U46C\_K48A}$, and GPX4$^{U46C\_K48L}$ (Cys46-SO$_3$H). All n=20,835 independent measurements of distances throughout the simulation time were plotted, with means ± SD. Unpaired two-tailed t test was then performed and P values were plotted.

h, Viabilities of HT1080 overexpressing exogenous WT, K48A, or K48L GFP-GPX4 and a control line were measured after treatment of IKE (0.6 μM) for 48 hours. Data are plotted as means ± SD, n=3 biologically independent samples. Two-tailed t tests were then performed and P values were plotted.
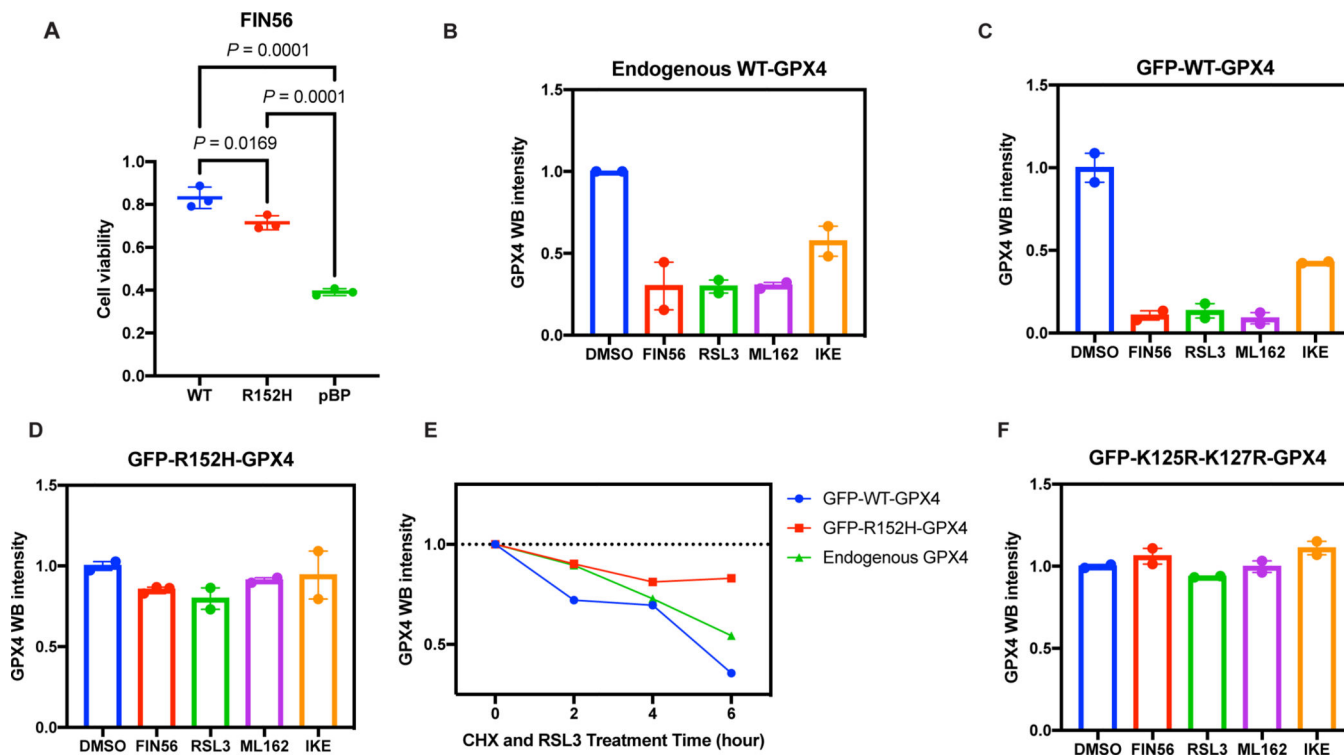
Figure 4. Resistance of GPX4[R152H] to degradation induced by GPX4 inhibitor revealed the Ubiquitin/Proteosome-dependent mechanism of the GPX4 degradation induced by FIN56/RSL3.

a, Viabilities of HT1080 overexpressing exogenous WT or R152H GFP-GPX4 and a control line were measured after treatment of FIN56 (0.6 μM) for 48 hours. Data are plotted as means ± SD, n=3 biologically independent samples. Two-tailed t tests were then performed for comparison and P values were plotted.

b, The endogenous GPX4 in HT1080 OE GFP-WT-GPX4 were tested for vulnerability to the degradation induced by RSL3, ML162, FIN56, and IKE. Data are plotted as means with range of two biologically independent experiments. The corresponding blots are shown in Extended Data Figure 4b and 4c.

c, The GFP-WT-GPX4 in HT1080 OE GFP-WT-GPX4 were tested for vulnerability to the degradation induced by RSL3, ML162, FIN56, and IKE. Data are plotted as means with range of two biologically independent experiments. The corresponding blots are shown in Extended Data Figure 4e.

d, The GFP-R152H-GPX4 in HT1080 OE GFP-R152H-GPX4 were tested for vulnerability to the degradation induced by RSL3, ML162, FIN56, and IKE. Data are plotted as means with range of two biologically independent experiments. The corresponding blots are shown in Extended Data Figure 4f.

e, Cycloheximide chase analysis of GFP-WT-GPX4, GFP-R152H-GPX4, and endogenous WT GPX4. Means of two biologically independent experiments were plotted. The corresponding blots are shown in Extended Data Figure 4g.

f, The GFP-K125R-K127R-GPX4 in HT1080 OE GFP-K125R-K127R-GPX4 were tested for vulnerability to the degradation induced by RSL3, ML162, FIN56, and IKE. Data are plotted as means with range of two biologically independent experiments. The corresponding blots are shown in Extended Data Figure 4h.
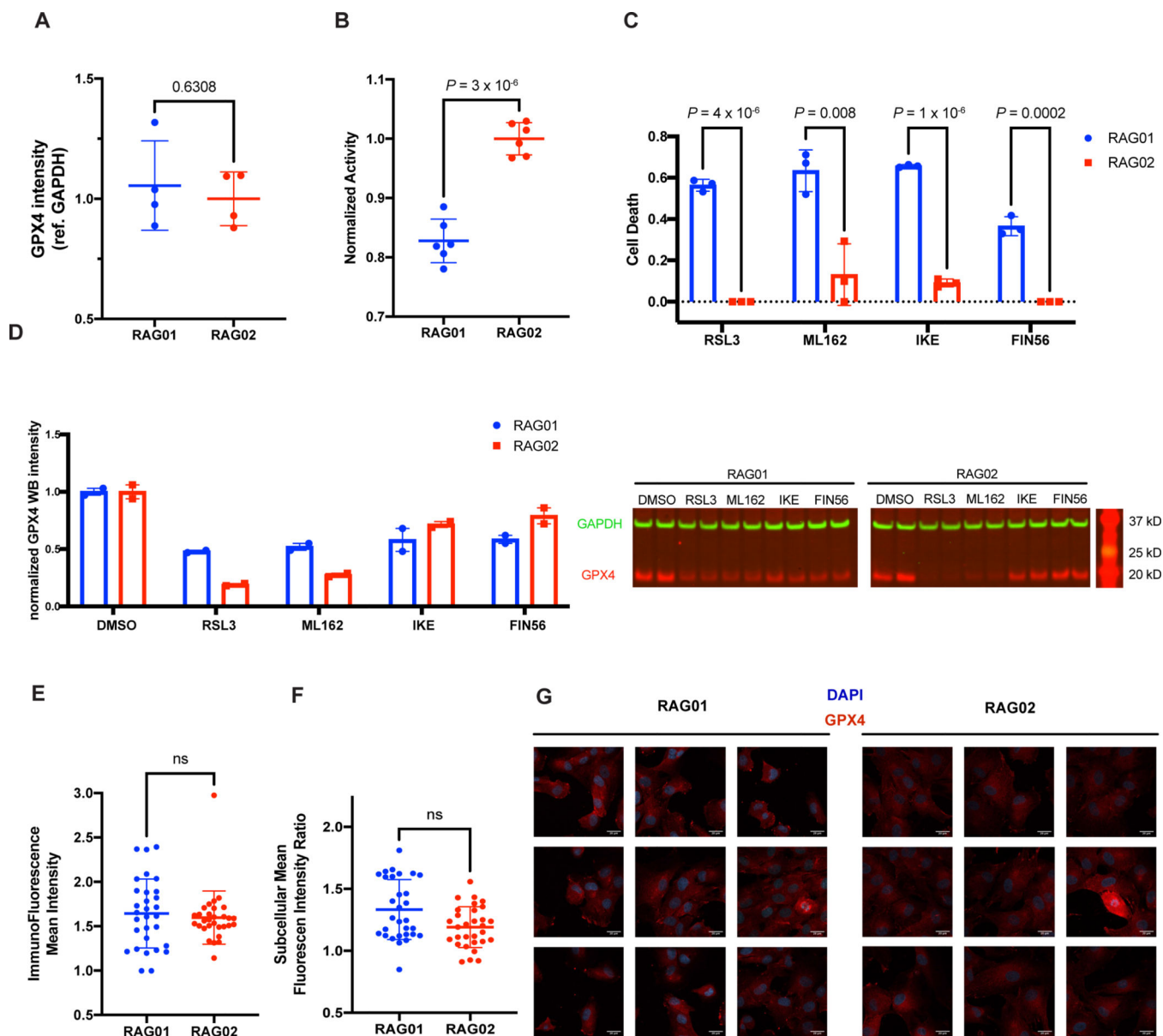
Figure 5. Pathology analysis was validated in the patient fibroblasts.

a, RAG01 (patient, with homozygous R152H mutation in GPX4) and RAG02 (parent of patient, with heterozygous R152H mutation in GPX4) were tested for GPX4 protein expression level by WB. Data are plotted as means ± SD (n=4 biologically independent samples). Unpaired two-tailed t test was then performed: t=0.5061, df=6 and P value was plotted.

b, Activity of GPX4 in RAG01 and RAG02 was measured in an NADPH-coupled GPX4 activity assay. Data are plotted as means ± SD (n=6 biologically independent samples). Unpaired two-tailed t test was then performed: t=9.212, df=10 and P value was plotted. See methods of cell culture for discussion on effects of α-tocopherol.

c, Viabilities of RAG01 and RAG02 were measured after treatment of RSL3 (4 μM), ML162 (4 μM), IKE (30 μM), and FIN56 (500 μM) for 24 hours. Data were plotted as means ±

SD, n=3 biologically independent samples. Ordinary two-way ANOVA followed by Sidak's multiple comparisons test was performed and P values were plotted: n=3, DF=16.

d, RAG01 and RAG02 were tested for vulnerability to GPX4 degradation induced by 10 μM RSL3, ML162, FIN56, and IKE. Data are plotted as means with range in the left panel (n=2 biologically independent samples). Western blots are shown in the right panel. Full scan image is shown in the supplemental information.

e, Mean cellular immunofluorescence of GPX4 observed in RAG01 and RAG02. Data are plotted as means ± SD (n=30 biologically independent samples). Unpaired two-tailed t test was then performed and plotted: t=0.5155, df=58, P^{ns}=0.6081.

f, Ratio of mean cytoplasm immunofluorescence of GPX4 over mean nuclear immunofluorescence of GPX4 observed in RAG01 and RAG02. Data are plotted as means ± SD (n=30 biologically independent samples). Unpaired two-tailed t test was then performed and plotted: t=1.846, df=58, P^{ns}=0.0713.

g, Nine representative immunofluorescence images for RAG01 and RAG02 were presented, showing DAPI (blue) and GPX4 fluorescence (red). Scale bar is corresponding to 20 μm.
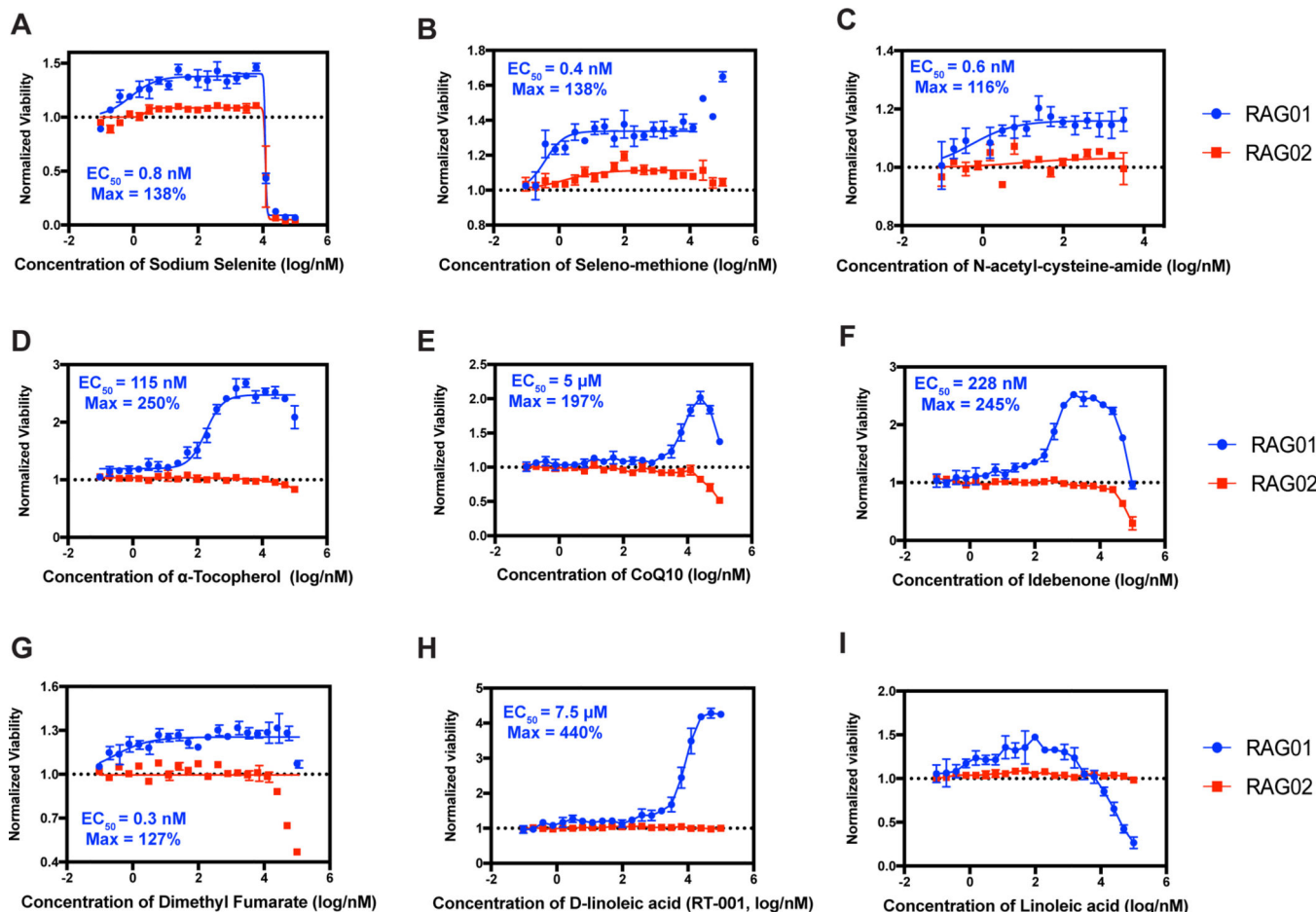
Figure 6. Proof-of-concept treatments on patient fibroblast.
Supplementations of sodium selenite (a), selenol-methione (b), N-acetyl-cysteine-amide (c), α-Tocopherol (d), CoQ10 (e), idebenone (f), dimethyl fumarate (g), D-linoleic acid (h), and linoleic acid (i) were tested as proof-of-concept treatments on the patient and control fibroblasts. α-Tocopherol was removed from medium in advance and the fibroblast cells were treated with proof-of-concept treatments on Day 5 without α-Tocopherol Increase of cell number was monitored over control fibroblast cells treated with DMSO only. Data are plotted as means ± SD (n=3 biologically independent samples).